PAPER

Check for updates

Copper(II) chelates of a coumarin-based acyl hydrazone ligand: structural characterization and computational evaluations for prospective applications in antimicrobial, antiviral, antioxidant, and anticancer therapies†

Manar. S. Mahfouz, Amira A. M. Ali, Magdy Shebl, Omima M. I. Adly [ID] and R. Fouad [ID] *

This study represents the synthesis and comprehensive characterization of four novel copper(II) chelates (CuR, CuRCT, CuH, and CuHCT) derived from a newly developed coumarin-based acyl hydrazone ligand (HCBH). The chelates were prepared using multidisciplinary synthetic routes, including reflux and hydrothermal methods with or without surfactant assistance, resulting in distinct mono- and binuclear structures with nanoscale morphologies. Structural analyses confirmed that all copper complexes possess tetrahedral geometries, with ligand coordination modes varying between tridentate and tetradentate depending on the synthetic method. TEM imaging revealed unique morphologies for each chelate, and the successful dispersion of the bioactive CuH chelate into silica yielded a porous nanostructured drug delivery system. Biological evaluations revealed promising antimicrobial activity, particularly for CuHCT against E. coli and S. aureus, and for CuRCT against B. subtilis and C. albicans. Antioxidant assays showed that CuRCT and CuHCT exhibited superior activity compared to other complexes and standard ascorbic acid. CuH demonstrated potent cytotoxicity against HepG-2 and MCF-7 cancer cell lines, comparable to cisplatin, while maintaining moderate toxicity toward normal Vero cells ($CC_{50} = 43.34 \pm 1.98$ μg ml^{-1}). Although the antiviral activity of CuH against HAV was weak, in vitro release studies of CuH–silica composites confirmed controlled release behavior, supporting its potential as a nanodrug delivery system. Density Functional Theory (DFT) and molecular docking analyses corroborated the biological findings, with favorable interactions observed between the compounds and CDK2 kinase. Collectively, these results highlight CuH as a highly promising candidate for further preclinical evaluation, especially in cancer therapy, with silica-based dispersion enhancing its potential as a nanocarrier for targeted drug delivery.

1. Introduction

In recent years, one of the most actively pursued areas of coordination chemistry has been the creation and production of novel nano-chelates with various morphologies, particularly distinctive structures, and significant pharmacological properties for the potential treatment of cancer, viral, and microbial diseases. The pharmacological properties of metal chelates are influenced by several factors, including the type of metal ions used, the selective bioactive chelating agents, the morphology, particle size, surface area, and the method employed to prepare

the chelates.[1,2] Among bioactive chelating agents, coumarins, known as benzopyran-2-ones, feature a simple and versatile structure, with the benzopyrone ring as their central framework. This core structure enables coumarins to interact with various enzymes and receptors through non-covalent interactions.[3] As a result, coumarins exhibit a broad spectrum of biological activities, including anticancer,[4,5] anti-inflammatory,[6,7] antimicrobial,[8,9] and antithrombotic[10,11] effects. Copper ions and copper-based metallodrugs have been extensively explored for their biochemical activities within biological systems, primarily due to copper's diverse roles as an essential endogenous trace metal. Copper ions can bind to proteins, including albumin and ceruloplasmin. Moreover, copper is characterized by its high redox activity, wide structural variability, bioavailability, and its capacity to promote the generation of reactive oxygen species (ROS).[12,13] Furthermore, the intricate relationship between copper and cancer cell proliferation has spurred investigations

Department of Chemistry, Faculty of Education, Ain Shams University, Roxy, 11711, Cairo, Egypt. E-mail: Raniaahmed@edu.asu.edu.eg; Fax: +20 (02) 22581243; Tel: +20 01000212207

† Electronic supplementary information (ESI) available. See DOI: https://doi.org/10.1039/d5ra03317a

into the development of Cu-binding ligands aimed at regulating tumor tissue homeostasis.[14] Additionally, copper chelates are thought to be effective alternatives to platinum-based medications and potential antitumor agents, in addition to their activity as chemical nucleases, enzyme inhibitors, or antiviral, antimicrobial, and anti-inflammatory agents. They promote an alternative on-apoptotic mechanism of programmed cell death by inducing oxidative stress towards DNA through the formation of ROS.[12] Nanoparticles can be utilized to deliver medications by changing signal transduction or modifying the tumor microenvironment, and they also enable the sustained and regulated delivery of anticancer treatments.[15] Particle size, shape, and surface chemistry are examples of physicochemical characteristics of nanoparticles that have been found to significantly impact drug delivery and cellular toxicity.[16] Efforts have been undertaken to improve the biological features of nano-chelates by modifying their production process. Nano-chelate synthesis techniques have so far drawn a lot of scientific attention since various synthetic processes can alter the morphology and other biological characteristics of the materials that are generated. Hydrothermal, reflux, microwave, and other synthesis procedures have been introduced to achieve the unique biological features of the nano-chelates. The hydrothermal and reflux procedures in particular are quite alluring among these techniques since they are inexpensive, safe, effective, and have the potential to be environmentally friendly and large-scale manufacturing processes.[2] Moreover, the control of crystalline size, distribution, and morphology can be effectively achieved through the addition of counter ions, capping molecules, hydrothermal temperature adjustments, and processing time. The choice of an appropriate stabilizer is crucial in the synthesis process to prevent excessive aggregation of nanoparticles (NPs).[17] In this context, surfactants are often preferred over other capping agents due to their ability to form micelles, their excellent solubilization properties, and their ease of removal from the surfaces of NPs. Cetyltrimethylammonium bromide (CTAB) is an amphiphilic compound that possesses both hydrophobic and hydrophilic characteristics, along with a non-toxic nature.[18] In light of the aforementioned findings, this study presents a green synthesis of copper(II) nano-chelates (**CuR, CuRCT, CuH, CuHCT**) from a newly synthesized 3-acetyl coumarin-based ligand (**HCBH**) using hydrothermal and reflux methods, with or without CTAB. The resulting nano-chelates showed spherical morphologies with diverse nanoscale dimensions and particle distributions, influenced by reaction conditions, and were structurally confirmed *via* comprehensive characterization. Biologically, the chelates exhibited broad-spectrum antimicrobial and strong antioxidant activities. Notably, **CuH** showed significant anticancer effects against HepG-2 and MCF-7 cell lines, with moderate cytotoxicity on normal Vero cells. Although its antiviral activity against HAV was limited, embedding **CuH** in a silica matrix enabled a controlled drug release profile. Molecular docking with CDK2 and DFT calculations supported their anticancer potential, positioning these nano-chelates as promising candidates for further therapeutic development.

2. Methodology

2.1. Materials

Reagent-grade chemicals included salicylic acid hydrazide,[19] 3-acetyl coumarin,[20] methyl salicylate (Sigma-Aldrich, 99%), ethyl acetoacetate (Sigma-Aldrich, 99%), salicylaldehyde (Sigma-Aldrich, 99.5%), and hydrazine hydrate (Sigma-Aldrich, 99%). Copper acetate salt, glacial acetic acid, ethylenediamine tetraacetic acid (EDTA) disodium salt, Tris–HCl, 2,2-diphenyl-1-pikryl-hydrazyl (DPPH), ascorbic acid, cetyltrimethylammonium bromide (CTAB), tetraethyl orthosilicate $Si(OC_2H_5)_4$ (TEOS), ammonium hydroxide, metal indicators, and nitric acid were BDH or Merck. Organic solvents were used as high-quality reagents.

2.2. Characterization

Microanalyses of nitrogen, hydrogen, and carbon were conducted at the Micro-analytical Center of Cairo University, Giza, Egypt. The metal content in the chelates was quantified through complexometric analysis. Melting and decomposition points were determined using a Stuart melting point apparatus (England). Molar conductivities were measured using a Corning conductivity meter (model NY 14831) with 10^{-3} M solutions of the solid nano-chelates prepared in DMF. Thermogravimetric (TGA) and derivative thermogravimetric (DTG) analyses were performed on a Shimadzu thermogravimetric analyzer from room temperature to 800 °C, employing a heating rate of 10 °C per minute. Fourier-transform infrared (FT-IR) spectra of **HCBH** and its copper chelates, spanning a range of 4000–400 cm^{-1}, were recorded on a Nicolet IS10 FT-IR spectrometer. Proton nuclear magnetic resonance (^{1}H-NMR) spectra at 300 MHz were obtained using a Mercury-300BB spectrometer, with tetramethylsilane (TMS) as an internal standard and dimethyl sulfoxide (DMSO) or DMSO-d$_6$ as solvents. UV-vis absorption spectra for 10^{-3} M solutions of the solid nano-chelates in DMF were measured using a JASCO V-550 UV-vis spectrophotometer. Magnetic susceptibility measurements were conducted at room temperature using a Sherwood Scientific magnetic susceptibility balance (Cambridge Science Park, England) and the Gouy method. The effective magnetic moments (μ_{eff}) were calculated using the relation $\mu_{eff} = 2.828$ (cm T)$^{1/2}$ B.M., where cm denotes the molar susceptibility, corrected using Pascal's constants to account for the diamagnetic contributions of all atoms in the compounds. Electron spin resonance (ESR) spectra were recorded with a Bruker X-band spectrometer (model EMX). X-ray diffraction (XRD) patterns were obtained using a PHILIPS diffractometer with CuKα_1 radiation ($\lambda = 1.54056$ Å), operating at an emission current of 30 mA and an accelerating voltage of 40 kV. Transmission electron microscopy (TEM) images were captured using a JEOL JEM-2100 TEM instrument at an accelerating voltage of 200 kV.

2.3. Synthesis

2.3.1. Synthesis of 2-hydroxy-N'-(1-(2-oxo-2*H*-chromen-3-yl)ethylidene)benzohydrazide ligand (HCBH). The 2-hydroxy-N'-(1-(2-oxo-2*H*-chromen-3-yl)ethylidene)benzohydrazide (**HCBH**)

was synthesized through the condensation of salicylic acid hydrazide stoichiometrically in a molar ratio 1 : 1 with 3-acetyl coumarin in absolute ethanol. The mixture was refluxed for two hours. The reaction mixture was allowed to cool fully to room temperature before separating the yellow crystals. Ethanol recrystallization created fine crystals when the product was filtered away (Scheme 1).

2.3.2. Synthesis of copper(II) nano-chelates

2.3.2.1. Synthesis of CuR nano-chelate. An aqueous solution of copper(II) acetate was added to a methanolic solution of **HCBH** to produce **CuR** chelate. Eight hours were spent refluxing the reaction mixture. The resulting precipitate was filtered and rinsed with a 50% (v/v) methanol–water mixture to remove any remaining unreacted starting material residues. Ultimately, anhydrous $CaCl_2$ was used to dry the precipitate overnight in vacuum desiccators.

2.3.2.2. Synthesis of CuRCT nano-chelate. The **CuRCT** was synthesized by the same previous method of preparation of **CuR**, in addition to adding CTAB surfactant (1 mM) before the refluxing step.

2.3.2.3. Synthesis of CuH nano-chelate. In a 100 ml Teflon-lined autoclave with 70% filling, a mixture of **HCBH** and copper(II) acetate was dissolved in water and heated to 120 °C for 24 hours. Deep brown crystals were produced once the reactor gradually cooled to room temperature. After being filtered out, the crystals were cleaned with distilled water and allowed to dry at room temperature over anhydrous $CaCl_2$ in a desiccator.

Scheme 1 Schematic representation of hydrazone ligand (**HCBH**).

2.3.2.4. Synthesis of CuHCT nano-chelate. The chelate **CuHCT** was prepared as the previous method except for adding CTAB (1 mM). Very fine brown crystals were obtained. The chemical formula of the dried copper chelates was collected in Scheme S1.†

2.3.2.5. Synthesis of the CuH nano-chelate silica xerogel nanohybrid. Initially, a silica matrix that contains **CuH** nano-chelate was obtained by the sol–gel process.[21] Then **CuH** nano-chelate (0.031 g) was dissolved in DMSO (5 ml). Then 0.1 ml of the complex solution was added to 10 ml of the silica sol to obtain a 10^{-4} M solution of the **CuH** nano-chelate in silica sol. Then the solution was stirred for 2 h at room temperature. Finally, a transparent sol was obtained after stirring, which lasted for 24 h till the gel formed. The gel is dried at 80 °C for 6 h.

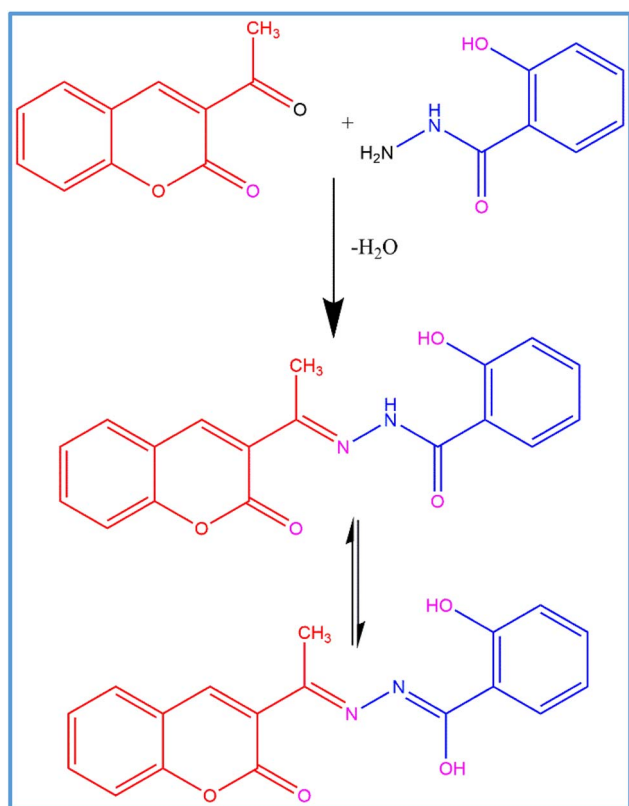## 2.4. Investigation of biological activity

2.4.1. Antimicrobial activity

2.4.1.1. Agar well diffusion method. The antimicrobial activities of under-investigated compounds were studied using the agar diffusion method[22] against three types of bacteria: *Staphylococcus aureus* and *Bacillus subtits* (Gram-positive bacteria) and *Escherichia coli*, (Gram-negative bacteria) using nutrient agar medium. The antifungal activity of the compounds was tested against *Candida albicans*. Antimicrobial activity was assayed by measuring the diameter of the inhibition zone formed around the well. Ampicillin and Gentamicin were standard drugs for Gram-positive and Gram-negative bacteria, respectively. Nystatin was used as a standard drug for fungi strains.

2.4.1.2. Minimum inhibition concentration (MIC) test. Series concentrations of **CuH** nano-chelate were tested against *E. coli* (Gram-negative-bacteria). The MIC value defined as concentration, which causes complete inhibition (no visible microbial growth), was detected.[23]

2.4.2. Antioxidant activity.
Using a UV-vis spectrophotometer, the antioxidant activity of **HCBH** and its copper chelates was assessed using the published methodology.[24] As a reference standard, ascorbic acid was employed. Using the relation IC_{50} (%) $= [(A_o - A_t)/A_o] \times 100$, where A_t is the tested sample's absorbance value and A_o is the blank sample's absorbance value, the tested samples' radical scavenging activity, represented as a percentage inhibition of DPPH, was determined. Plotting the percent inhibition at 30 and 60 minutes against log concentration allowed for the calculation of the IC_{50} value using the linear equation. Finding the IC_{50} values: the percentage inhibition and log concentration were fitted using linear regression. The IC_{50} value was defined as the concentration at which 50% inhibition occurred. Greater antioxidant activity means a lower IC_{50} value.

2.4.3. Antitumor activity.
The *in vitro* cytotoxic impact (IC_{50}) of the produced **HCBH** and its copper nano-chelates using viability assay was assessed following the literature approach[25,26] on two cancer cell lines: hepatocellular carcinoma cell line (HepG-2) and human breast cancer cells (MCF-7). Standard cisplatin was used to compare the findings

obtained. The survival curve of each tumor cell line following treatment with the specified substance is obtained by plotting the relationship between surviving cells and drug concentration. Graphic plots of the dosage response curve for each concentration were used to estimate the 50% inhibitory concentration (IC_{50}), which is the concentration needed to produce toxic effects in 50% of intact cells.

2.4.4. Antiviral activity

2.4.4.1. Mammalian cell line. The Vero cells which were provided from the American Type Culture Collection, were taken from the kidney of an African green monkey (ATCC, Manassas, VA, USA). The Vero cells were grown in Dulbecco's modified Eagle's medium (DMEM), which was enhanced with 50 μg per ml gentamycin, 10% heat-inactivated fetal bovine serum (FBS), 1% L-glutamine, and HEPES buffer. Every cell was incubated twice a week at 37 °C in a humidified environment with 5% CO_2.[27]

2.4.4.2. Virus propagation. Confluent Vero cells were used to propagate and test the cytopathogenic HAV virus.[28] The Spearman–Karber method was used to count the infectious viruses by calculating the 50% tissue culture infectious dose (TCID50) with eight wells per dilution and 20 μl of inoculum per well.[29]

2.4.4.3. Cytotoxicity evaluation. The Vero cell lines were used to assess the cytotoxicity assay. The MTT colorimetric technique was used to determine the cell viability.[30] The 50% cytotoxic concentration (CC_{50}), or the concentration required to cause lethal effects in 50% of intact cells, was estimated to use graphical plots of each conc's dose–response curve. A test for cytopathic effect inhibition was used to screen for antivirals. In sensitive mammalian cells, this assay was chosen to demonstrate a cytopathic effect, or particular suppression of a biological function, as determined by the MTT technique. To determine the viral inhibition rate, the formula was [(A − B)/(C − B)] × 100%, where A, B, and C stand for the tested chemicals' absorbance with virus-infected cells, the virus control's absorbance, and the cell control's absorbance, respectively.[30]

2.4.5. Drug delivery.

Weight 0.01 g of the **CuH** nano-chelate dispersed into silica and dissolved in a solution containing 1% DMSO and 99% phosphate-buffered saline (PBS, pH 7.4). The solution was incubated at 37 °C using a thermostat shaker. After incubation, centrifuge the solution and take filtrate to measure absorbance after 0, 1, 2, 3, 7, 10, 12, 24, 28, and 32 h. The concentration of **CuH** nano-chelate dispersed into silica in the release media was detected by ultraviolet spectrophotometer.

2.5. Theoretical study

2.5.1. DFT calculations.

At the B3LYP level of theory, Density Functional Theory (DFT) was used to optimize the molecular structures of the **HCBH** ligand, and its copper nano-chelates.[31,32] For the non-metal atoms (C, H, N, and O), a 6-311G(d,p)[33] was used, and for the metal centers, a LANL2DZ.[34] Frontier molecular orbitals, namely the Lowest Unoccupied Molecular Orbital (LUMO) and the Highest Occupied Molecular Orbital (HOMO), might be calculated using this method. Then, using established equations from the literature,[35] key electronic

characteristics were determined, such as energy gap (ΔE), electronic chemical potential (μ), chemical hardness (η), electrophilicity index (ω), and softness (σ).

2.5.2. Molecular docking simulations.

AutoDock Vina, a well-known tool for evaluating binding interactions, was used to carry out the molecular docking technique for the drugs under study.[36] The crystal structure of CDK-5 inhibitors, more especially the inhibitor EFP bound to CDK-2 (PDB ID: 3IG7), which was obtained from the Protein Data Bank (PDB),[37] was the study's goal. To optimize the protein for docking, polar hydrogen atoms, and Kollman charges were added after water molecules, ligands, and heteroatoms were eliminated from the receptor (PDB ID: 3IG7).[38] Chem Draw was first used to sketch the compounds, and following energy minimization, the MDL format was changed to PDBQT. The docking grid box was carefully specified with dimensions ($X = 4.493$ Å, $Y = 11.804$ Å, $Z = 12.061$ Å) and coordinates ($X = 0.862$, $Y = 28.53$, $Z = 7.321$) to provide precise binding site evaluation. The compounds' affinities for the receptor were assessed by calculating their binding energies, which offered comprehensive information on how the ligands and the target protein interacted.[39] The potential biological significance of the investigated compounds is supported by this rigorous methodology, which makes it possible to comprehend the binding affinities and modes fully.

3. Results and discussion

3.1. Structural descriptions of HCBH ligand

The condensation of 3-acetyl coumarin with salicylic acid hydrazide results in the formation of a hydrazone ligand in the form of 2-hydroxy-N'-(1-(2-oxo-2H-chromen-3-yl)ethylidene) benzohydrazide (**HCBH**) as shown in Scheme 1. The displayed chemical formula $C_{18}H_{14}N_2O_4$ is consistent with the elemental analysis data. **HCBH** is air-stable and soluble in organic solvents such as DMSO and DMF. Fig. S1† shows the FT-IR spectrum of **HCBH** and provides valuable information on the structure of the generated ligand. The **HCBH** can exhibit keto/enol tautomerism due to its acyclic amide (NH–C=O) functional group. The presence of the ν(NH) band at 3260 cm^{-1} and the ν(C=O) band at 1640 cm^{-1} indicates that the **HCBH** is still in its keto form.[40] Moreover, the **HCBH** exhibits a noticeable band at 1724 cm^{-1} due to ν(C=O)$_{lactone}$ stretches.[41] Furthermore, the (C=N) group is responsible for the band at 1572 cm^{-1}.[42,43] The ν(OH) group is represented by the broad band, which is visible at 3469 cm^{-1}.[44]

^{1}H-NMR spectrum analysis verified the production of the **HCBH**. The ^{1}H-NMR spectrum of **HCBH** (Fig. S2†) showed singlet signals at δ 14.18, and 11.39 ppm, which could be connected to OH$_{phenolic}$ and NH$_{amide}$, respectively, and vanished when D_2O was introduced (Fig. S2b†).[40] Aromatic moieties' protons have been found to exhibit multiplets in the 6.84–8.27 ppm range.[40] Also, the signal that appeared at 2.28 ppm has been associated with the methyl group.

For the electronic spectrum of the chelating agent (**HCBH**), the absorption band (highest energy) corresponding to π–π* transitions of the aromatic ring system appeared at 274 nm (Fig. S3†).[45] An additional band (moderate energy) observed at

331 nm may be associated with n–π* transitions within C=O and C=N groups.[46]

3.2. Structural and thermal descriptions of copper nano-chelates

The **CuR** and **CuRCT** chelates are obtained directly by a reflux treatment, whereas the hydrothermal treatment achieved the **CuH** and **CuHCT** chelates. Elemental analysis, FT-IR spectroscopy, ESR spectra, molar conductivity, magnetic moment measurement, UV-vis spectroscopy, and thermogravimetric analysis (TGA) were used to investigate the copper chelates. Table S1† lists the physical, analytical, and molar conductance data of the prepared compounds. The prepared nano-chelates (**CuR**, **CuRCT**, **CuH** and **CuHCT**) are colored, stable, and non-hygroscopic. These chelates are soluble in DMF and DMSO but insoluble in methanol and ethanol. The suggested chemical structure of copper nano-chelates is validated by elemental analysis. Scheme S1† shows that **CuR** and **CuRCT** have a 1 : 1 molar ratio and the chelates involved copper ions with a coordination number of four. Acetate ion occupies one of the four coordination sites as a monoanionic monodentate group, whereas **HCBH** occupies the other three sites. Furthermore, the **HCBH** chelating agent acts as a monobasic tridentate through the O-atom of lactone, the N-atom of azomethine group, and the O-atom of a deprotonated hydroxyl group. While **CuH** and **CuHCT** have a 2 : 1 molar ratio (Cu^{2+} : **HCBH**), the chelates involved two copper ions each of them surrounded by four coordination sites. The acetate group occupies two of four coordination sites as monoanionic bidentate group whereas

HCBH occupies two other coordination sites. **HCBH** functions as a bis-bidentate monobasic in **CuH** and **CuHCT** chelates through the O-atoms of lactone, N-atom of azomethine group, and oxygen of deprotonated hydroxyl and phenolic groups. Molar conductance values of 10^{-3} M of **CuRCT** and **CuR** nano-chelates (in DMF) are too low and fall within the typical range of non-electrolytes without ionic acetate groups. Under identical conditions, the molar conductance value for **CuH** and **CuHCT** nano-chelates fell within the range typical of a 1 : 1 electrolyte (Table S1†). This confirms the presence of one acetate anion as a counter ion out of the coordination sphere.[47–49]

To gain insights into the thermal degradation mechanisms of the prepared chelates and to investigate the existence of solvent molecules, the copper chelates were subjected to thermogravimetric analysis (TGA). The scheme of temperature-induced degradation and the steps involved in the thermal degradation of copper nano-chelates are shown in Schemes S2 and S3.† Fig. 1 shows the TGA–DTA curves of copper nano-chelates. The findings agreed with the theoretical formula that the analytical data indicated. In the first stage, **CuR** nano-chelate loses one coordinated acetic acid molecule at 312.5 °C (weight loss 13.30%; calcd 13.52%). In the second step, the complex loses CH_4, HCN, and CO_2 molecules at 437.5 °C (weight loss 33.14%; calcd 33.15%). For **CuRCT**, the half molecule of non-coordinated water was released at 106 °C (weight loss 1.82%; calcd 1.98%). The following stage of **CuRCT** is related to removing a coordinated acetic acid molecule at 316.5 °C (weight loss 15.35%; calcd 15.24%). The third step corresponds to the loss of CH_4, HCN, and CO_2 molecules with a weight loss of
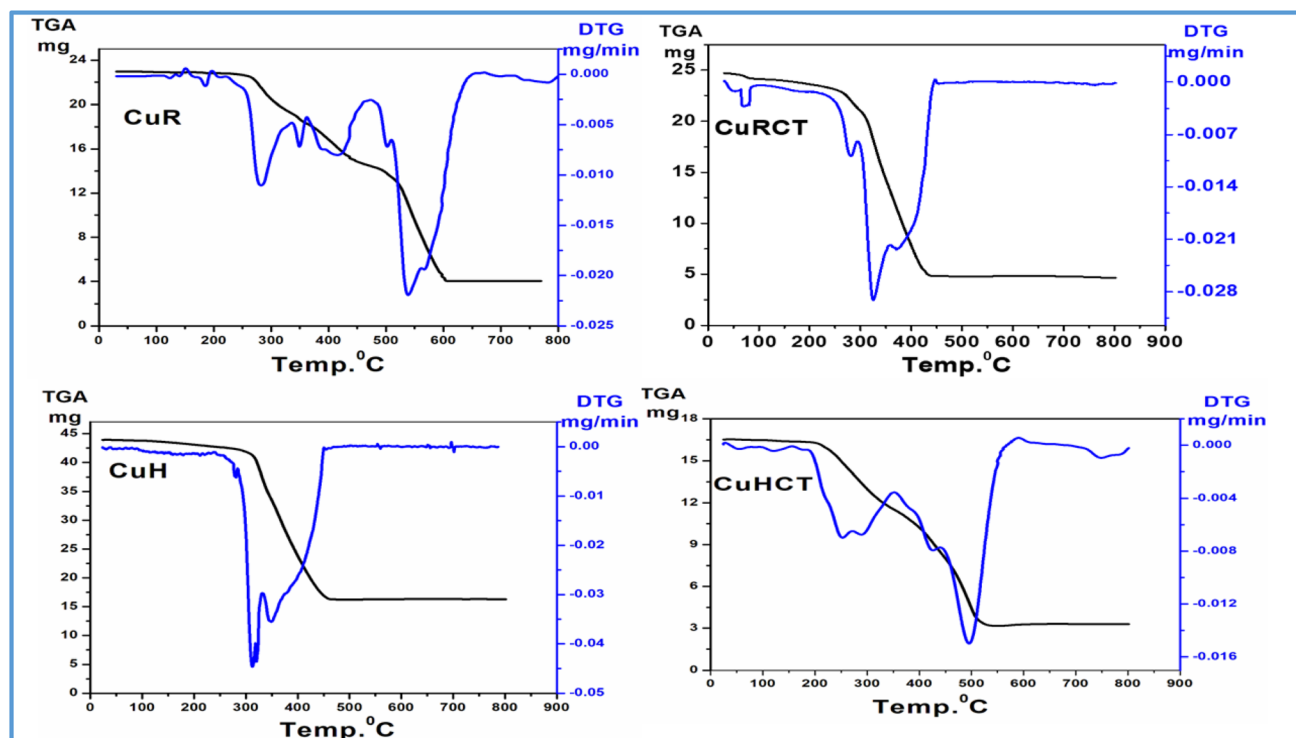

Fig. 1 TGA–DTA curves of **CuR**, **CuRCT**, **CuH** and **CuHCT** nano-chelates.

34.44% (calcd 34.48%). **CuH** nano-chelate loses uncoordinated acetic acid at 314 °C (weight loss 9.44%; calcd 9.60%) followed by coordinated two acetic acid molecules at 385 °C (weight loss 28.54%; calcd 28.80%). For **CuHCT** the uncoordinated acetic acid was removed at a temperature of 240 °C (weight loss 9.31%; calcd 9.60%). Then the two coordinated acetic acid molecules were released at 379 °C (weight loss 28.33%; calcd 28.80%). The isolated copper chelates completed their degradation to reach the final residue CuO: found; (calcd) 17.91% (17.63%), CuO: found; (calcd) 18.10% (17.56%), 2CuO and 6C: found; (calcd) 37.11% (36.94%) and Cu$_2$O: found; (calcd) 22.51% (22.87%) for **CuR**, **CuRCT**, **CuH** and **CuHCT** respectively.

The thermodynamic parameters governing the decomposition processes of complexes, including the activation energy (ΔE), enthalpy (ΔH), entropy (ΔS), and Gibbs free energy change (ΔG), were systematically evaluated through graphical analysis utilizing the Coats–Redfern equation. This method has proven effective in determining the reaction order (n) and activation parameters for the primary degradation stages of both the ligand and metal complexes.[50] The kinetic parameters are listed in Table S2.† The following observations can be made based on the analysis: (i) the degradation processes are endothermic, as indicated by the positive values of enthalpy change (ΔH). (ii) For **CuR** and **CuRCT** chelates, the decomposition rate of the second degradation step is faster than the first step, as evidenced by lower activation energy (ΔE) values for the second step compared to the first step. Conversely, for **CuH** and **CuHCT**, the activation energy for the second degradation step is higher, suggesting that the second stage of decomposition occurs more slowly[51] (iii) the activated chelate formed during the degradation process exhibits a more ordered structure than the reactants, or the reactions are relatively slow, as shown in the negative entropy change (ΔS) values for the complexes.[52] Relatively, low positive ΔG values indicate the autocatalytic effect of metal ions on the thermal degradation of the chelates, suggesting that the degradation processes are non-spontaneous.[53]

3.3. Spectroscopic description of copper nano-chelates

3.3.1. FT-IR spectral descriptions.
Table S3† lists the significant infrared absorption bands along with their corresponding assignments. The **HCBH** ligand participates in coordination *via* enol form which is confirmed by (i) the disappearance of a characteristic, strong amide carbonyl group (C=O)$_{amide}$ in all copper nano chelates. (ii) The band of NH$_{amide}$ which appeared at 3260 cm^{-1} in the **HCBH** disappeared in all copper nano chelates due to deprotonation of the NH group during the tautomerization process. (iii) Additionally, by deprotonating the NH group, new bands of (C=N)$_{enolic}$ in the 1510–1520 cm^{-1} appeared in copper nano chelates, suggesting the coordination *via* enol form instead of through keto form. Moreover, the most noticeable alteration of spectral features of **HCBH** when coordinated to copper ion is the downward shift of the lactonic carbonyl group to the extent of about 30–31 cm^{-1}, which indicates that the metal is coordinated to the oxygen of lactonic carbonyl. Also, new bands corresponding to ν(M–O) bonds (514–585 cm^{-1}) confirm the participation of lactonic

carbonyl in coordination.[54] Moreover, the (C=N)$_{azomethine}$ group suffered a positive shift of about 12–22 cm^{-1} in copper nano-chelates, indicating the participation of these groups in complexation. The emergence of non-ligand bands at the 433–454 cm^{-1} regions, which are assigned (M–N) bonds, subsequently confirms the presence of the azomethine group in the chelating arms.[55] The **CuR** and **CuRCT** nano-chelates exhibit new bands in the ranges 1486–1487 and 1255–1256 cm^{-1}, which may be due to asymmetric and symmetric vibration modes of the acetate group, respectively. The large difference between the two bands (>200 cm^{-1}) illustrates the monodentate nature of the acetate group.[56,57] On the other hand, **CuH** and **CuCTH** nano-chelates exhibit new bands in the ranges 1434–1478 and 1301–1313 cm^{-1}, which may be due to asymmetric and symmetric vibration modes of the acetate group, respectively. The relatively small difference between ν_{as} and ν_s bands clearly illustrates the bidentate nature of the acetate group.[58]

3.3.2. Absorption spectra and magnetic properties.
The electronic spectra of the chelating agent (**HCBH**) and its copper nano-chelates are collected in Fig. 2. The electronic absorption spectra of **CuR**, **CuRCT**, **CuH**, and **CuHCT** nano-chelates exhibit an absorption band at 684, 675, 632, and 646 nm, respectively. The $^2T_{2g}$–^2E_g transition of tetrahedral copper chelates is responsible for these bands.[59,60] The difference in absorption character bands can be attributed to the different crystal sizes, and morphologies[2] (see later Section 3.4). The magnetic moment values of **CuR**, **CuRCT**, **CuH**, and **CuHCT** (per copper atom), are 2.01, 2.10, 1.84, and 1.89 B.M., respectively which validate the tetrahedral geometry value.[59,60] In addition, the magnetic moment value of all cationic species (μ_{comp}) in **CuH** and **CuHCT** equal 2.59 and 2.67 B.M, respectively, which confirms the proposed structure (binuclear chelates).

3.3.2.1. Stability of compounds.
Thermodynamic stability over extended periods is a critical parameter for evaluating potential drugs. All candidate drugs must maintain stability under physiological conditions to effectively reach their target within living organisms. The stability of copper nano-chelates was assessed in a water/DMSO solution (10 μM, 0.1% DMSO) using UV-vis spectroscopy. Time-dependent UV-vis spectra of the **CuH** chelate, selected as a representative example, were recorded at specific time intervals (0, 2, 6, 12, 24, and 72 hours) in the water/DMSO solution, as illustrated in Fig. S4.† The spectral characteristics and peak absorptions remained consistent over time, indicating the absence of any structural modifications in the chelates. Additionally, the nano-chelates were measured electronically using Nujol mulls and DMF solutions. The minimal impact of DMF on the chelate configuration is demonstrated by the spectra and band positions of all chelates in DMF solutions are roughly identical to those observed as Nujol mulls. Demonstrating that the same species exists in both solid and solution forms further supports the idea that complexes maintain their integrity in solutions.

3.3.3. ESR spectra.
The ESR spectra reveal comprehensive details on the type of metal–ligand interactions and stereochemistry. The room temperature ESR spectra of copper nano-chelates are shown in Fig. S5.† The shape of the ESR signals exhibits one signal in the tetrahedral structure of the copper
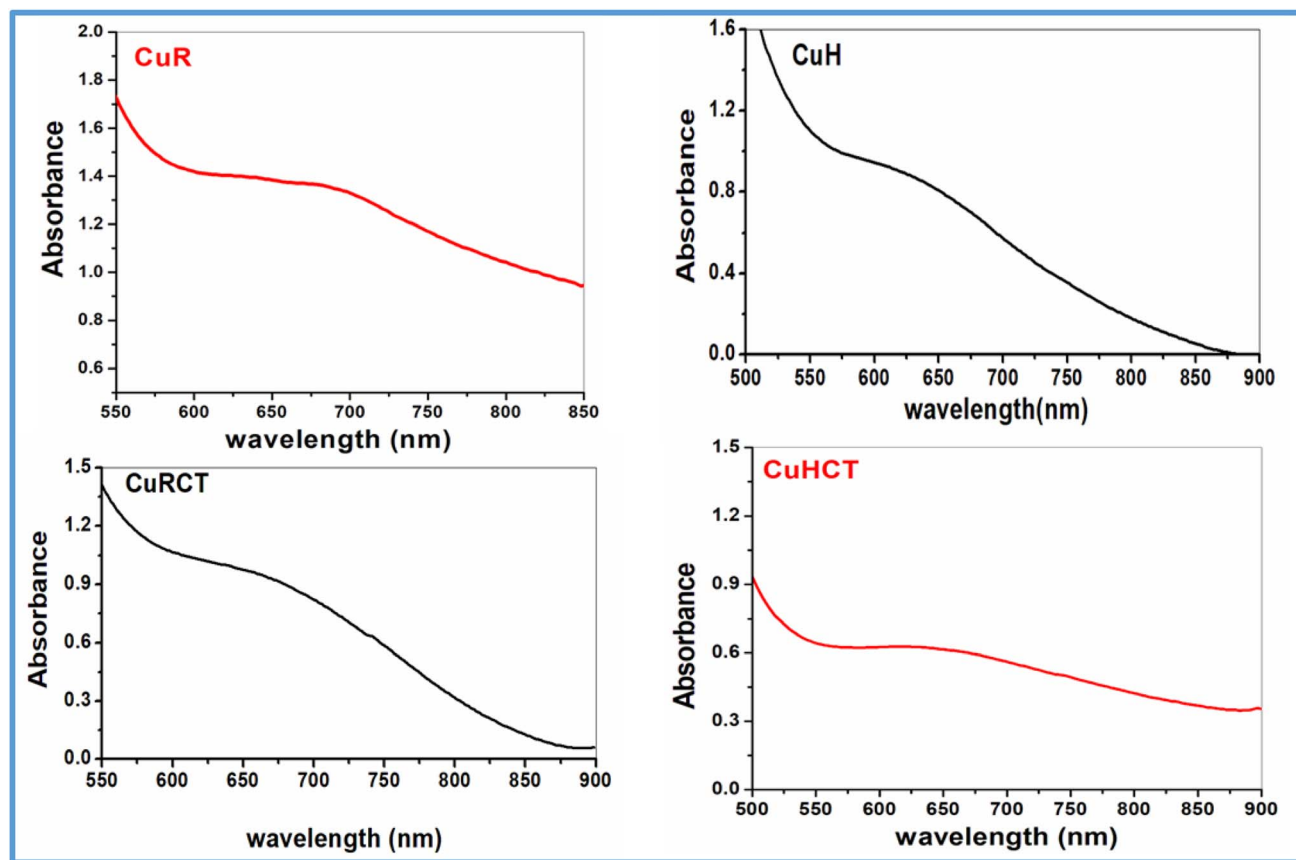
Fig. 2 UV-vis spectra of CuR, CuRCT, CuH and CuHCT nano-chelates.

nano-chelates.[60] The detected g values of the **CuR, CuRCT, CuH,** and **CuHCT** are $g_{eff} = 2.075, 2.075, 2.051,$ and $2.073,$ respectively.

3.4. Morphological description (TEM study)

The TEM image of **CuR** chelate shows the hybrid morphology of connected nanospheres (an average diameter of 23 nm) and nanorods (an average diameter of 27 nm with several lengths) (Fig. 3). A high separate uniform accumulated spherical particles formed a spherical cluster with an average size of 73 nm appeared in the case of **CuRCT** chelate (Fig. 3). Also, as represented in the TEM image of **CuH** Fig. 3, the particles of **CuH** have uniform and separated spherical shapes with an average size of 8 nm. On the other hand, **CuHCT** has an aggregated spherical shape with an average diameter of 29 nm. It is clear from Fig. 3 that the treatment methods (reflux and hydrothermal) with or without surfactant (CTAB) during the preparation process might influence the morphology and crystal sizes of copper chelates.

TEM image of **CuH** chelate dispersed into silica exhibited porous sheet morphology with an average pore diameter of 18 nm. In silica pores, **CuH** chelate is evenly dispersed (Fig. S6†). These findings clarify that the **CuH** chelate particles were restricted to the silica pores' internal region preventing the development of crystals larger than the pore domain.

CTAB significantly alters morphology. The reason for this is that during the preparation phase, CTAB formed micelles that confined the particles within their micelle chamber. Small spherical CTAB structures lower than CMC (critical micelle concentration) can be used to explain the shape-directing function of CTAB; these sub-micellar aggregates can physically interact with the reactants to generate active entities.[61] The following mechanism could be used to explain how aggregated and accumulated spherical nanoparticles of chelate form during the addition of CTAB with hydrothermal or reflux processes. Once CTAB-assisted reflux or hydrothermal process, the organic ligand was solubilized by the surfactant micelles through electrostatically attracting of the positive heads of CTAB and electron-donating groups of organic ligand like C=N and –OH groups.[62] In **CuRCT** chelate, the electrostatic interaction is more prevalent due to the presence of free OH groups. This interaction slows down the ligand–Cu^{2+} ion reaction rates and further regulates the morphologies of the resulting nano-complex. Copper ions are not attracted to CTAB alone. However, there is a greater chance of interaction between the copper ion and the organic ligand's donating group than there is with the nano-complex that forms. Accordingly, micelles serve as nucleating sites for the development of spherical crystals of nano-chelate (Scheme 2). A portion of the CTAB molecule is released when the nano-chelate grows to particles, while other molecules adsorb on the surface of the chelate particle by
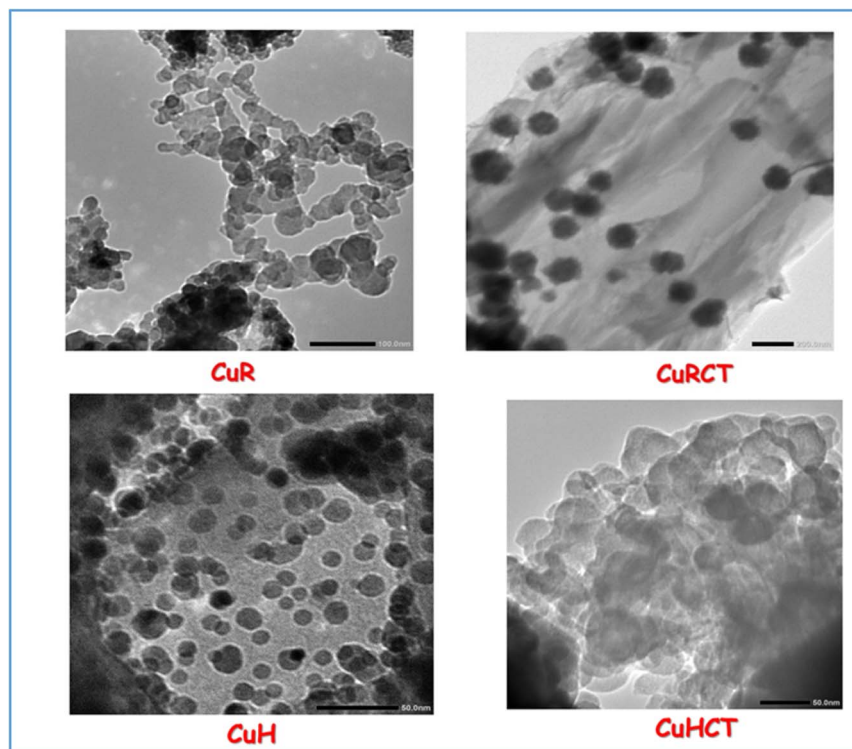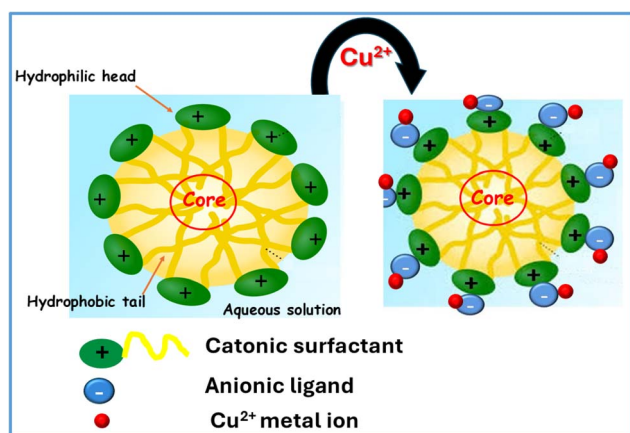
Fig. 3   TEM images of **CuR**, **CuRCT**, **CuH** and **CuHCT** nano-chelates.

Scheme 2   The schematic mechanism of the possible formation of **CuRCT** and **CuHCT** nano-chelates.

hydrogen bonding with the free phenolic –OH group. Thus, the higher accumulated spherical complex particles are formed as seen from TEM analysis. As shown from Scheme S1,† the structure of **CuHCT** is binuclear without a free phenolic group, but the structure of **CuRCT** has a free phenolic group which confirms the separately accumulated spherical chelate particles higher than the previous complex (TEM images).

3.5.   Biological properties descriptions

3.5.1.   Antimicrobial properties

3.5.1.1.   Inhibition zone's diameter investigation. The antibacterial and antifungal properties of **HCBH** and its synthesized copper nano-chelates were investigated using the agar diffusion method[22] in DMSO solvent against various bacterial species, including Gram-positive bacteria (*Staphylococcus aureus* and *Bacilus subtilis*) and Gram-negative bacteria (*Escherichia coli*), using nutrient agar medium. The antifungal activity of the compounds was tested against *Candida albicans* using Sabouraud dextrose agar medium. Standard drugs for the Gram-positive and Gram-negative bacteria were Ampicillin and Gentamicin, respectively, while nystatin was used for the fungal strains. Table 1 displays the results, which are reported as the inhibition zone's diameter. A good comparability between the studied chelates and common antibacterial agents is also displayed in Table 1. Except for Gram-negative bacteria (*Escherichia coli*), the chelating agent (**HCBH**) is ineffective against all other bacteria and fungi. Each of the copper nano-chelates showed a different level of growth inhibition on the tested bacterial and fungal species. However, antimicrobial activity of all nano-chelates varied from high to moderate activity compared with standard antibiotics. **CuR** < **CuH** < **CuRCT** < **CuHCT** was the order that inhibited *E. coli* and *S. aureus* the most, according to the findings in Fig. S7.† Therefore, using the prepared nano-chelates to treat some common disorders caused by *S. aureus* and *E. coli* seems reasonable. **CuR** < **CuH** < **CuHCT** < **CuRCT** is the order in which the nano-chelates inhibit *B. subtits*. **CuRCT** also exhibits a discernible antifungal effect against *Candida albican*. From the above findings, it is observed the coordination enhances the antibacterial activity of the copper chelates, which is superior to that of the **HCBH** ligand. These findings may be explained according to Overton's concept and chelation

Table 1 The antimicrobial activity of HCBH and its copper chelates[ab]

Sample Microorganism	HCBH	CuR	CuRCT	CuH	CuHCT	Standard antibiotic
Gram negative bacteria						Gentamicin
Escherichia coli (ATCC: 10536)	7.3 ± 1.0	9.3 ± 0.6	12.7 ± 0.6	11.7 ± 0.6	13.7 ± 0.6	27 ± 1.0
Gram positive bacteria						Ampicilin
Staphylococcus aureus (ATCC: 13565)	NA	14.3 ± 0.6	19.0 ± 1.0	17.3 ± 0.6	21.3 ± 0.6	21.0 ± 1.0
Bacilus subtits (DSM: 1088)	NA	11.3 ± 0.6	19.3 ± 0.6	17.0 ± 1.0	18.7 ± 0.6	21.3 ± 0.6
Fungi						Nystatin
Candida albicans (ATCC: 10231)	NA	9.3 ± 0.6	11.7 ± 0.6	10.0 ± 1.0	9.0 ± 1.0	21.0 ± 1.0

[a] Zone of inhibition is expressed as mean ± standard deviation (mm). [b] NA: no activity, well diameter 6 mm, 100 µl was tested.

theory. The chelates have a great chance of acting as more potent and stronger fungicidal and bactericidal drugs due to the chelation between the ligand and the metal ion, destroying more bacteria and fungus than the ligand as a result. In particular, the presence of a metal's positive charge that is partially shared with the donor group causes the π–electron to delocalize throughout the entire chelating system. According to Overton's theory of cell permeability, a key factor causing antimicrobial action is liposolubility. Chelation makes coordinated molecules more lipophilic, which improves metal chelate penetration into lipid membranes and prevents additional microbial growth. Metal coordinates also impact the respiration process of cells, which prevents protein synthesis and impedes the organism's ability to grow. Additionally, the activity of various complexes against various bacteria varies depending on either the ribosome variations in microbial cells or the impermeability of the bacteria's cells.[63,64]

Furthermore, antimicrobial activity was affected by various factors like geometry, morphological structure, and particle size of under-studied compounds. These factors may be responsible for the variety of antimicrobial activity of the prepared copper nano chelates. Although **CuR** and **CuRCT** have the same geometry, the **CuRCT** recorded higher activity than **CuR**. Also, **CuHCT** showed higher activity than **CuH**. That may be due to the effect of CTAB which leads to an increase in the hydrophobic and lipophilic character of the chelates, consequently, enhancing the permeability to the microbial cells and killing the organisms effectively.

Also, it is shown that **CuH** has higher antimicrobial than **CuR**. This could be attributed to the smaller nanoparticle size, which enhances its spreading to microbial cells.

3.5.1.2. MIC investigation. Series concentrations of highly antimicrobial active copper nano-chelates (**CuHCT** and **CuRCT**) were tested against *B. subtits* and *S. aureus* and (Gram-positive bacterium), *E. coli* (Gram-negative bacterium) and *C. albicans* (fungi). The concentration that results in complete inhibition (no discernible microbial growth) is known as the MIC value.[23,65,66] **CuHCT** recorded stronger antimicrobial action against *S. aureus* with MIC of 31.25 µg ml^{−1} with respect to **CuRCT** (MIC of 62.5 µg ml^{−1}) and standard Ampicillin (MIC = 62.5 µg ml^{−1}). Also, the **CuHCT** and **CuRCT** show weak activity

against *E. coli* (MIC = 250 µg ml^{−1}), *B. subtits* (MIC = 250 µg ml^{−1}) and *C. ablicans* (MIC = 125 µg ml^{−1}).

3.5.2. Radical scavenging (antioxidant) activity. A simple, reliable, and affordable method for evaluating the antioxidant capacity of various substances is the DPPH assay.[24] It depended upon the decay of DPPH˙'s main absorption band in the visible spectrum. The DPPH˙ scavenging arises from electron or hydrogen donation in the case of a structure that donates hydrogen or electrons, and its absorbance decreases over time. DPPH assay of the produced **HCBH** and its copper nano-chelates was detected and compared with a standard compound (ascorbic acid). For every compound, concentration-dependent free radical scavenging properties were calculated (Fig. 4). The increasing scavenging assay is a function of the concentration of prepared nano-chelates. Scheme S4† shows the color change of DPPH from purple to yellow after mixing with **CuR** as a representative example. The appearance of a yellow color may be attributed to the forming of a hydrazine form of DPPH due to the chemical reduction. The antioxidant activity of chelates depends on (i) the presence of conjugation (ii) the existence of coordination sites like azomethine nitrogen (C=N), lactonic oxygen (C=O), and phenolic group (OH) where the reactivity of free radical can be neutralized by the donation of an electron or hydrogen.[67] The **HCBH** records a significantly high antioxidant activity due to the presence of various free functional groups. Among the copper nano-chelates that were
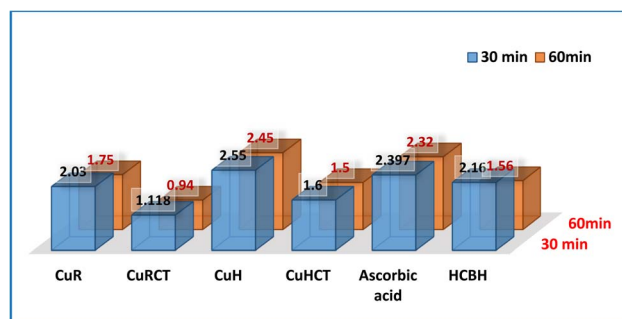

Fig. 4 IC$_{50}$ of HCBH, CuR, CuRCT, CuH, CuHCT nano-chelates and standard ascorbic acid at 30 min and 60 min.

investigated, the strongest antioxidant activity was shown by the **CuRCT** (IC$_{50}$ = 1.11 μM). Similar to the **CuRCT**, the **CuHCT** nano-chelate exhibited strong free radical scavenging activity (IC$_{50}$ = 1.60 μM). Copper chelates with CTAB (**CuRCT** and **CuHCT**) show more antioxidant activity than pure copper chelates (**CuR** and **CuH**), although the chemical structures of chelates are comparable. It is assumed that the positively charged CTAB headgroups attract copper chelate stabilizing of oxidized products intermediate *i.e.*, antioxidants in the free radical forms, and this process leads to the accumulation of the copper chelate anion in the interfacial region.[68,69]

3.5.3. Cytotoxicity activity (*in vitro* test). The viability assay assessed the *in vitro* cytotoxic effects of the synthesized **HCBH** and its copper chelates against two cancer cell lines: human breast cancer cells (MCF-7) and human liver cancer cells (HepG-2). The **HCBH** recorded lower activity relative to its copper chelates and standard cis-platin against HepG-2 and MCF-7 cell lines with IC$_{50}$ = 75 and 113 μg ml^{-1}, respectively. Fig. 5 records the relation between % cell viability and concentration of **CuR**, **CuRCT**, **CuH**, and **CuHCT** nano-chelates for the detection IC$_{50}$ of the compounds. As shown in Fig. S8† the copper chelates recorded high antitumor activity against HepG-2 with the order of **CuH** (IC$_{50}$ = 1.19) < **CuHCT** (IC$_{50}$ = 2.18) < **CuR** (IC$_{50}$ = 7.65) < **CuRCT** (IC$_{50}$ = 12.28 μg ml^{-1}). Regarding the human breast cancer cells (MCF-7), the values of IC$_{50}$ of **CuR**, **CuRCT**, **CuH**, and **CuHCT** are 11.74, 17.12, 1.93, and 3.86 μg ml^{-1}, respectively. The results show that the current nano-chelates are more active than the **HCBH**. This implies that coordination enhanced the anticancer impact. According to Tweedy's chelation theory, the cytotoxic potency may be explained by the metal's positive charge increasing the acidity of the coordinated ligand with protons. This results in stronger hydrogen bonds, which promote biological activity.[2] The prepared copper nano-chelates have remarkably high cytotoxicity. The variety of IC$_{50}$ values of the prepared copper nano-chelates may be due to different

factors, like the percentage of metal ions, free functional groups, and conjugation. In humans, copper is a necessary trace element. The two oxidation states of copper ions Cu(I) and Cu(II) ions are involved in some physiological processes. Cell damage and copper-induced cell death can result from a persistent copper imbalance that raises the concentration of copper inside cells.[70] There are two main components to the functions of copper ions: first, the Fenton reaction produces a significant amount of reactive oxygen species (ROS), which damages DNA and causes lipid peroxidation. Second, by inducing aggregation in lipoylated, binding interactions prevent mitochondrial metabolic activity. Ultimately, this encourages copper-dependent apoptosis in cells.[71,72] Moreover, the free function group bearing a proton such as phenolic –OH leads to stronger hydrogen bonds and enhances the antitumor activity.[2] The conjugation also enhances growth-inhibitory activity, where the conjugation often increases the therapeutic effect, alters a toxicity profile, and/or selectively targets the therapeutic agent to the tissue of interest.[73] Moreover, biological activity is affected by significant factors such as particle size and shape. The crystal size of the current nano-chelates is inside the nanoscale, as shown by the TEM investigation. As shown in Scheme S1,† **CuH** and **CuHCT** contain two copper ions. This may be the reason for higher antitumor activity than other prepared chelates. Although **CuH** nano-chelate has the same chemical structure (contains two copper ions), **CuH** exhibits higher antitumor activity. This may be due to the morphology and size properties of **CuH** nano-chelate. TEM results show that **CuH** is characterized by a highly dispersed spherical morphology with smaller particle sizes than **CuHCT**. This increases the facility of its uniform penetration and distribution into tumor cell.[2] Although **CuR** and **CuRCT** have the same geometry, **CuR** has higher antitumor activity. This may be regarding spherical morphology, and the smaller nano-size of **CuR**. In the case of **CuRCT**, the morphological structure is an
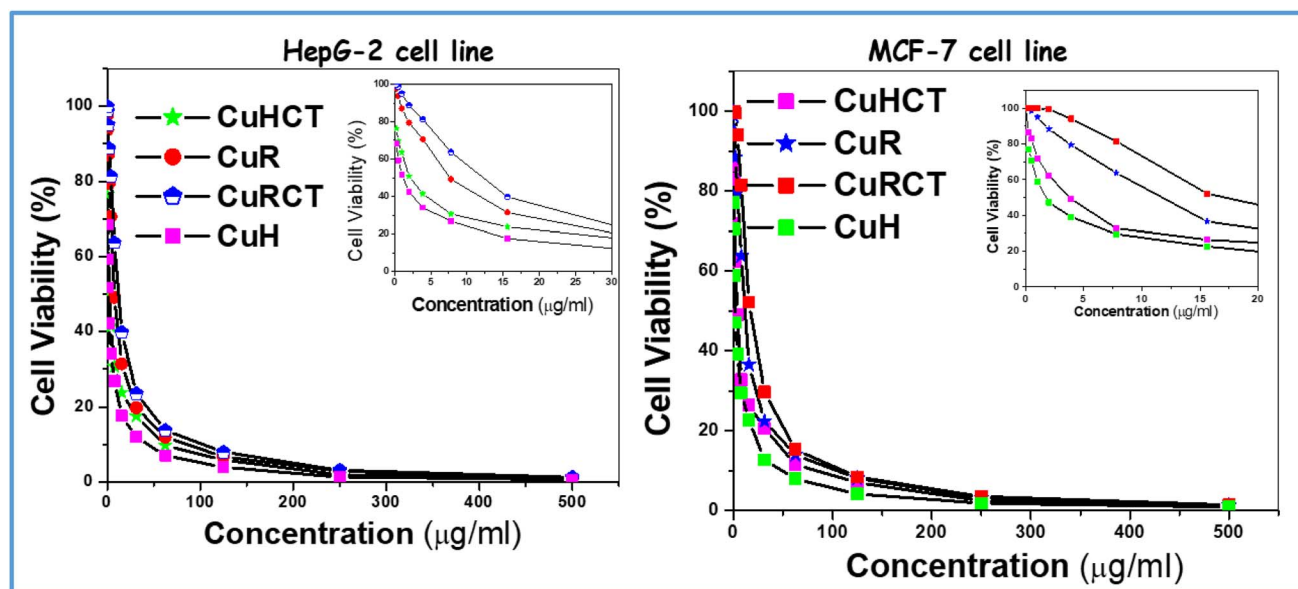

Fig. 5 Relation between cell viability and concentration of HCBH, CuR, CuRCT, CuH, and CuHCT nano-chelates.

accumulated spherical particle forming a large spherical cluster which hinders its penetration into tumor cells. As the afore-mentioned findings demonstrate, cytotoxic studies carried out on cell lines yield crucial data regarding the anticancer poten-tial of medications. The current compounds have the potential to function as efficient tumor inhibitors. These results suggest that the **CuH** nano-chelate could be an appropriate candidate for liver and breast anticancer medication in light of these findings. The potent anticancer drug of the prepared chelate (**CuH**) was dispersed into silica, and its cytotoxic activity against HepG-2 cell line was examined ($IC_{50} = 8$ μg ml^{-1}). The initial observation of cytotoxic value suggests that the **CuH** nano-chelate exhibits higher activity compared to that embedded into silica. However, examining these values closely reveals the opposite: the **CuH** dispersed into silica demonstrates superior cytotoxic activity. This enhanced activity is attributed to the low concentration of the **CuH** nano-chelate embedded within silica matrix, as detailed in the experimental section. The cytotoxic activity is evaluated based on the concentration of the **CuH** nano-chelate thus it becomes evident that the **CuH** dispersed into silica displays the highest cytotoxic effect. It is important to note that the IC_{50} concentration for the pure **CuH** nano-chelate reflects its full concentration, whereas in the case of the **CuH** dispersed into silica, the concentration corresponds to the **CuH** nano-chelate (very low concentration) combined with silica matrix. This distinction underscores the significant cytotoxic efficiency of the **CuH** dispersed into silica relative to the pure form.

3.5.4. Cell viability alteration. First, to evaluate the toxicity of bioactive **CuH** nano-chelate, VERO cells were needed for subsequent antiviral tests. The cytotoxic activity against Mammalian cells from African Green Monkey Kidney (Vero) cells was detected using MTT assay with 50% cell cytotoxic concentration of **CuH** nano-chelate is $CC_{50} = 43.34 \pm 1.98$ μg ml^{-1}.

3.5.5. Antiviral activity evaluation. The antiviral screening was performed using a cytopathic effect inhibition assay. The antiviral activity of **CuH** nano-chelate against Hepatitis A virus (HAV) was measured. Fig. S9† shows the weak antiviral effects of **CuH** nano-chelate against Hepatitis A virus (HAV).

3.5.6. In vitro drug delivery. The highly bioactive **CuH** nano-chelate was utilized as a template drug and incorporated into a silica xerogel matrix, demonstrating a gradual release profile. The rate of release (*in vitro*) of the **CuH** nano-chelate from the silica xerogel was monitored using spectrophoto-metry. The sample was immersed in phosphate-buffered saline (PBS) at pH 7.4 and maintained at a controlled temperature of 37 °C. The absorbance of the resulting solution was measured over time to evaluate the release profile. Fig. 6 illustrates the release profile of the **CuH** from silica. The absorption peak intensity increased over time, indicating a diffusion-controlled drug release mechanism.[74] The **CuH** exhibited an initial burst release of approximately 17% within the first hour, releasing a significant portion of the drug during this period. This was followed by a gradual increase in cumulative release over the subsequent hours, eventually reaching a plateau at 32 hours (Fig. 6). In summary, the silica xerogel matrix exhibits a rapid
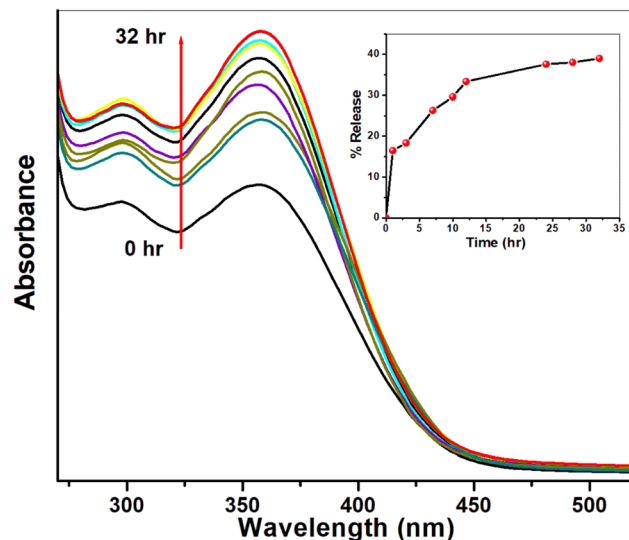

Fig. 6 The profile release of CuH nano-drug from silica xerogel matrix; (inset) the relation between % release of CuH nano-drug and time.

and substantial release in the early phase, followed by a sus-tained release of the **CuH** nano-drug governed by a diffusion-controlled mechanism. These findings highlight the potential of silica xerogel matrix for controlled release of the **CuH** nano-drug, demonstrating its effectiveness as a delivery system for cancer therapy.

3.6. Theoretical study

3.6.1. Molecular modeling. Density Functional Theory (DFT) with the B3LYP functional was used to simulate the molecules of **HCBH** and its copper nano-chelates (Fig. S10†) using the 6-311G(d,p) basis set for non-metal atoms (C, H, N, O) and the LanL2DZ basis set for the metal atoms. The Lowest Unoccupied Molecular Orbital (LUMO) and the Highest Occu-pied Molecular Orbital (HOMO) are two of the frontier molec-ular orbitals that are essential for assessing a molecule's chemical reactivity and transformational potential. The stability of chelates is significantly impacted by the energies of the HOMO and LUMO. In general, lower (more negative) HOMO and LUMO energies correlate with enhanced stability, as they reflect reduced reactivity and stronger electronic interactions within the chelate system. Table S4† lists the HOMO and LUMO energies for the compounds that are being studied. The spatial distribution of the HOMO–LUMO orbitals is depicted in Fig. S11,† with the positive and negative phases of these orbitals being shown in red and green, respectively. This visualization supports comprehending the distribution of electron densities and the areas most likely to engage in chemical reactions. Table S4† shows that the electronic characteristics of **HCBH**, and its copper chelates provide important information about their possible reactivity, which has important ramifications for noticed anticancer activities (Fig. S8†). The **HCBH** demonstrates relatively low HOMO energy (-6.26 eV) and a substantial energy gap ($\Delta E = 4.02$ eV), indicating reduced reactivity compared to its

copper chelates. A larger energy gap generally correlates with decreased chemical reactivity, implying that the **HCBH** ligand may have limited interaction with biological targets. Furthermore, the ionization potential of **HCBH** (IP = 6.26 eV) and electron affinity (EA = 2.24 eV) reflect moderate electronic stability. Its lower electronegativity (χ = 4.25 eV) and higher chemical hardness (η = 2.01 eV) further emphasize its resistance to electronic perturbations, supporting its stability under varying conditions. Specifically, the E_{HOMO} and E_{LUMO} characteristics show that **CuH/CuHCT** is probably more reactive than **CuR/CuRCT** because it has a higher HOMO energy (−8.22 eV) and a narrower energy gap (ΔE = 2.62 eV).[75] Higher HOMO indicates a greater capacity to donate electrons, whereas a smaller ΔE generally indicates greater chemical reactivity, which might improve interactions with biological targets such as cancer cells' cellular proteins.[76] The differences in electronic stability and reactivity are additionally expressed in the values of the electron affinity (EA) and ionization potential (IP).[77] Compared to **CuH/CuHCT**, **CuR/CuRCT** is comparatively less likely to lose electrons due to its greater IP (8.83 eV) and EA (5.98 eV).

CuR/CuRCT appears to be less reactive based on these characteristics as well as its higher electronegativity (χ) (7.40 eV) and chemical hardness (η) (1.42 eV). On the contrary, **CuH** is more polarizable and expected to interact with biological targets more easily due to its lower IP and higher softness (σ = 0.38). The greater reactivity and polarizability of **CuH/CuHCT** that promote binding interactions with cellular targets, support the higher antitumor activity (lower IC_{50} values) compared to **CuR/CuRCT** (Fig. S8†). These findings demonstrate how **CuH**'s electronic characteristics increase its chemical reactivity and suitability for improved interactions with cancer cell targets, which is consistent with its stronger anticancer efficacy. The relationship between electronic structure and biological efficacy

appears to have a mechanistic basis since the electronic configuration of **CuR/CuRCT** chelates seems to restrict its biological reactivity when compared to **CuH/CuHCT**. Table S4† collects the calculated E_{HOMO}, E_{LUMO}, energy gap (ΔE), ionization potential (IP), electron affinity (EA), electronegativity (χ), chemical potentials (μ), chemical hardness (η), softness (σ), and electrophilicity index (ω), by eV unit, of **HCBH** and its copper chelates.

Accurately predicting interactions in molecular docking studies requires an understanding of the distribution of partial charges on proteins and substrates. Maps of molecular electrostatic potential (MEP) are a crucial three-dimensional tool that graphically depicts molecular structure and charge distribution. Red denotes areas of negative charge (nucleophilic sites) and blue denotes areas of positive charge (electrophilic sites) in these maps.[78,79] For docking, researchers can rapidly identify important electrostatic characteristics and possible interaction positions on the protein and substrate owing to this color-coded arrangement.[80] The MEP map of the investigated compounds in Fig. 7 shows red regions surrounding electron-rich heteroatoms, indicating positions appropriate for electrophilic interactions, and blue regions which are usually seen around hydrogen atoms, observing the positions that could easily engage in intermolecular interactions with proteins. Our knowledge of chemical reactivity and interaction potential inside various molecular areas is enhanced by this imaging, which also provides guidance for docking and molecular recognition procedures.

3.6.2. Molecular docking simulation. The docking technique is essential for improving drug development by enabling a better comprehension of compound-target interactions and expediting the search for prospective therapeutic agents.[81] Cyclin-dependent kinases (CDKs) are a family of serine/threonine kinase enzymes that play critical roles in regulating
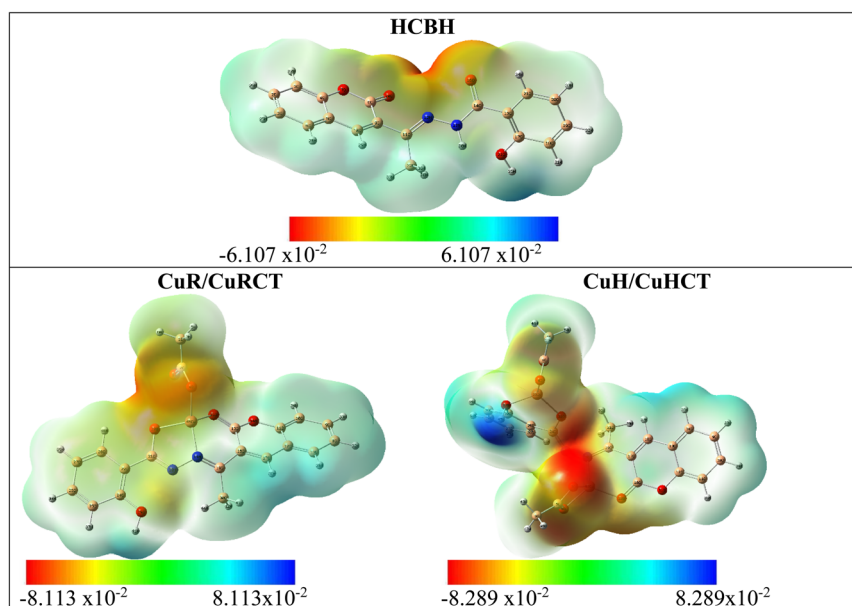

Fig. 7 Molecular electrostatic potential (MEP) map of the **HCBH** and its copper chelates.
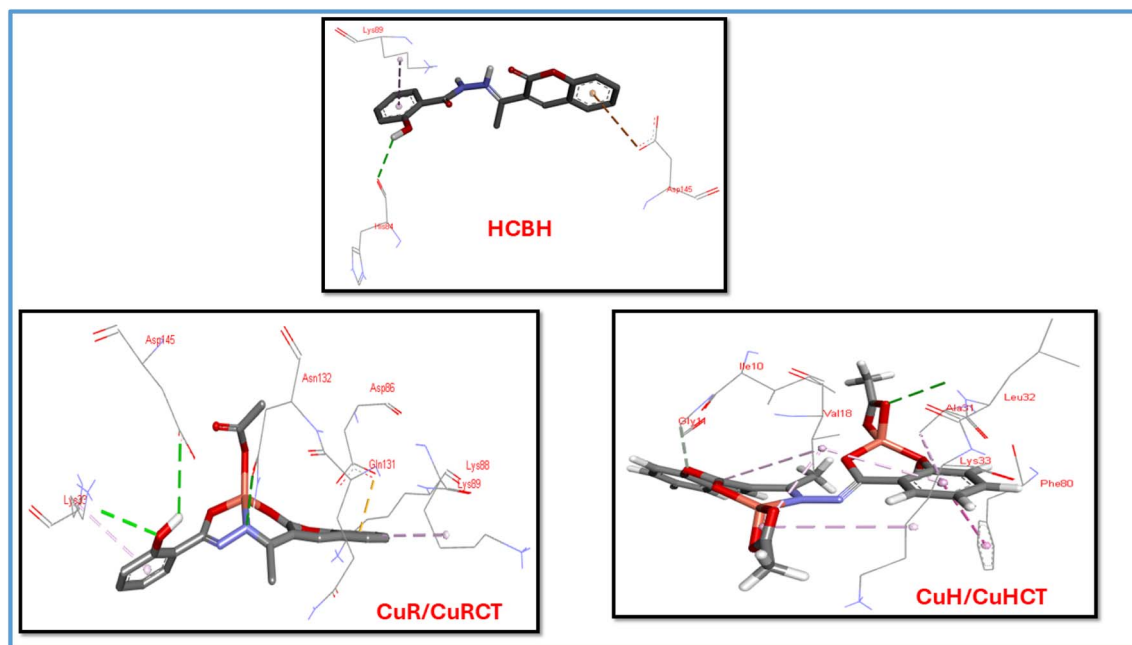
Fig. 8 3D representation of the hydrogen bonding between the studied compounds and the amino acid residues of the target protein (pdb ID: 3IG7).

cell division, transcription, and post-transcriptional modifications. Among them, CDK2 has emerged as a particularly promising therapeutic target for cancer treatment due to its pivotal role in cell cycle progression and its involvement in the proliferation of cancer cells.[82]

Firstly, *N*-(1-[*cis*-3-(acetylamino)cyclobutyl]-1*H*-imidazol-4-yl)-2-(4-methoxyphenyl)acetamide, the native ligand that was initially co-crystallized with the 3IG7 active site, was used in a re-docking and superimposition procedure to thoroughly validate the docking methodology. This co-crystallized ligand's binding pose was faithfully replicated during the validation, guaranteeing the dependability of the docking procedure. A high degree of alignment was seen when the re-docked ligand was superimposed with the native ligand, indicating that the docking process could accurately replicate the interactions of the original ligand within the active site. The durability and accuracy of the docking methodology are demonstrated by this successful validation, which is shown in Fig. S12.† As a result, it can be used to predict the binding modes of other drugs. To assess the binding interactions of the investigated drugs (**HCBH** and its copper nano-chelates), molecular docking was performed against the crystal structure of CDK-5 inhibitors, specifically the inhibitor EFP bound to CDK-2 (PDB ID: 3IG7). As shown in Fig. 8, the docking simulations identified the drugs' ideal binding modes. These docked patterns reveal information about the chemicals' interactions with the protein's active site. Table S5† provides a summary of the specific interactions with important amino acid residues. According to the molecular docking data, the **HCBH** and its copper nano-chelates with the target protein (PDB ID: 3IG7) exhibit different interaction profiles with different amino acid residues, which contribute to their binding energies and biological activities. The **HCBH**

forms a hydrogen bond with HIS84 at a distance of 2.75 Å, and a binding energy of -6.70 kcal mol^{-1}, As well as Pi–anion and Pi–alkyl interactions with ASP145 and LYS89, respectively. However, the binding of **HCBH** is relatively weaker compared to the nano-chelates. In contrast, **CuR/CuRCT** displays various strong interactions, including hydrogen bonds with LYS33, ASN132, and ASP145, with distances ranging from 2.54 Å to 3.00 Å, and a notable Pi–anion interaction with ASP86. These interactions lead to a stronger binding energy of -8.2 kcal mol^{-1}, indicating enhanced affinity toward the protein. For **CuH/CuHCT** exhibits the highest binding energy of -8.40 kcal mol^{-1}, driven by hydrogen bonds with LEU32 and GLY11, along with Pi–Pi interactions with PHE80 and multiple Pi–alkyl interactions, particularly with VAL18, demonstrating its strong interaction network. A pattern becomes apparent when comparing this molecular docking data with the *in vitro* cytotoxicity data. Poor antitumor effectiveness is indicated by the **HCBH** ligand's highest IC$_{50}$ value (71 μM) and weakest binding energy (-6.70 kcal mol^{-1}). On the other hand, **CuR/CuRCT** exhibits considerably better cytotoxicity and a stronger binding (-8.20 kcal mol^{-1}). **CuH/CuHCT** has the strongest binding (-8.40 kcal mol^{-1}) and the most varied interactions with the target protein. Its greater antitumor activity is reflected in its lowest IC$_{50}$ value. According to this relationship between binding energy and IC$_{50}$ values, these drugs' anticancer activity is probably going to be increased by greater interactions with the target protein.

4. Conclusion

This study developed eco-friendly copper(II) nano-chelates (**CuR**, **CuRCT**, **CuH**, **CuHCT**) from a coumarin-based ligand

(**HCBH**) using hydrothermal and reflux methods, with or without CTAB. Structural analysis confirmed tetrahedral geometries and coordination through ONO or ONOO donor sites. TEM showed morphology varied with synthesis conditions. Biologically, **CuHCT** had strong antibacterial effects (against *E. coli* and *S. aureus*), while **CuRCT** was effective against *B. subtilis* and *Candida*. Both **CuRCT** and **CuHCT** showed excellent antioxidant activity (IC$_{50}$: 1.11–1.60 μM). **CuH** displayed potent anticancer effects on HepG-2 and MCF-7 cells (comparable to cisplatin), with moderate toxicity on normal cells. Although **CuH** showed weak antiviral activity, encapsulation in silica improved its release profile. Computational studies (DFT, docking) supported its bioactivity. Overall, **CuH** is a strong antitumor candidate, and its silica nanohybrid offers a promising cancer drug delivery platform.

Data availability

Data are available on request from the authors.

Conflicts of interest

There are no conflicts to declare.

Acknowledgements

References

1 P. J. Dyson and G. Sava, Metal-based antitumor drugs in the post genomic era, *Dalton Trans.*, 2006, **16**, 1929–1933.

2 M. Saif, H. F. El-Shafiy, M. M. Mashaly, M. F. Eid, A. I. Nabeel and R. Fouad, Hydrothermal preparation and physicochemical studies of new copper nano-complexes for antitumor application, *J. Mol. Struct.*, 2018, **1155**, 765–775.

3 L. Gao, F. Wang, Y. Chen, F. Li, B. Han and D. Liu, The antithrombotic activity of natural and synthetic coumarins, *Fitoterapia*, 2021, **154**, 104947.

4 M. Shebl, T. E. Ali and M. A. Assiri, Novel mononuclear Cu(II), Ni(II), and Co(II) complexes of coumarinyl-pyrazolyl-thiazole thiosemicarbazone: Synthesis, characterization, and biological evaluation, *Appl. Organomet. Chem.*, 2025, **39**, e7948.

5 A. Benazzouz-Touami, k. Ighilahriz, M. Makhloufi-Chebli, N. Hadhoum, J. -Bernard Behr and A. Chouh, Synthesis, biological evaluation, ADMET studies, and molecular docking of novel coumarin–isoxazole derivatives as dual inhibitors of Hsp90 protein and acetylcholinesterase enzyme, *J. Mol. Struct.*, 2025, **1333**, 141776.

6 Y. Gong, X. Li, H. Tang, Y. Liu, S. Wang and Y. Geng, Synthesis, crystal structure, spectroscopic characterization, DFT calculations, Hirshfeld surface analysis, biological activity studies, molecular docking investigation, and ADMET properties evaluation of a novel 3-substituted coumarin derivative, *J. Mol. Struct.*, 2025, **1323**, 140739.

7 A.-S. Badran, M. A. Ibrahim and A. Ahmed, Nucleophilic reactions with the novel condensation product derived from 3-formylchromone and 4-hydroxycoumarin, *Syn. Comm.*, 2021, **51**, 1868–1881.

8 G. Yang, L. Shi, Z. Pan, L. Wu, L. Fan, C. Wang, C. Xu and J. Liang, The synthesis of coumarin thiazoles containing a trifluoromethyl group and their antifungal activities, *Arabian J. Chem.*, 2021, **14**, 102880.

9 M. S. Ebaid, M. Korycka-Machala, M. A. Shaldam, M. G. Thabit, M. Kawka, B. Dziadek, M. Kuziola, H. A. A. Ibrahim, X. Lei, A. I. Elshamy, J. Dziadek and A. Sabt, Exploring antitubercular activity of new coumarin derivatives targeting enoyl acyl carrier protein reductase (InhA): Synthesis, biological evaluation and computational studies, *J. Mol. Struct.*, 2025, **1336**, 142074.

10 K. Kasperkiewicz, M. B. Ponczek, J. Owczarek, P. Guga and E. Budzisz, Antagonists of vitamin K-popular Coumarin drugs and new synthetic and natural Coumarin derivatives, *Molecules*, 2020, **25**, 1465.

11 P. Karan, B. Shit, P. Panja, A. Khatun, M. Bera, J. Pal, S. Patra, S. Chakrabarti, S. Pal, A. Ghosh and M. Hossain, Synthesis of some new arylazo-coumarin derivatives and their comparative biological activity studies: Cytotoxicity, gene expression, DNA binding, BSAbinding, and *in silico* analysis, *J. Mol. Liq.*, 2025, **420**, 126813.

12 D. Ganci, L. D. Anna, G. Abruscato, M. L. Chevalier, O. Quideau, S. Cataldo, A. Pettignano, S. Rubino, R. Chiarelli, G. Barone, C. Luparello and R. Bonsignore, Harnessing redox reactions for anticancer effects: A copper(II) Schiff base complex induces apoptosis in HepG2 liver cancer cells *via* ROS generation, *J. Inorg. Biochem.*, 2025, **270**, 112938.

13 A. Kellett, Z. Molphy, V. McKee and C. Slator, *Recent Advances in Anticancer Copper Compounds: Metal-Based Anticancer Agents*, The Royal Society of Chemistry, 2019, pp. 91–119.

14 J. O. Pinho, I. V. Silva, J. D. Amaral, C. M. P. Rodrigues, A. Casini b, G. Soveral and M. M. Gaspar, circulating liposomes for colon cancer management, *Int. J. Pharm.*, 2021, **599**, 120463.

15 D. Chang, Y. Gao, L. Wang, G. Liu, Y. Chen, T. Wang, W. Tao, L. Mei, L. Huang and X. Zeng, Polydopamine-based surface modification of mesoporous silica nanoparticles as pH-sensitive drug delivery vehicles for cancer therapy, *J. Colloid Interface Sci.*, 2016, **463**, 279–287.

16 W. Hongdi, F. Jialing, L. Guijin, C. Baoqiong, J. Yanbin and X. Qiuling, *In vitro* and *in vivo* anti-tumor efficacy of 10-hydroxycamptothecin polymorphic nanoparticle dispersions: shape- and polymorph-dependent cytotoxicity and delivery of 10-hydroxycamptothecin to cancer cells, *Nanomedicine*, 2016, **12**, 881–891.

17 M. Mohammadikish and H. Hajisadeghi, Hierarchical crystal growth of sheaf-like CdS by microemulsion/hydrothermal route, *J. Mater. Sci.:Mater. Electron.*, 2017, **28**, 1455–1462.

18 I. M. A. Mohamed, Y. A. Khalifa, A. M. Shaker, L. Abdel-Mohsen and E. Nassr, Insights into the impact of surfactants on the kinetics of selenium nanoparticles formation *via* lemon juice-assisted methodology, followed by their antibacterial and antioxidant assessment, *J. Mol. Liq.*, 2024, **398**, 124241, DOI: 10.1016/j.molliq.2024.124241.

19 B. S. Furniss, A. J. Hannaford, P. W. G. Smith and A. R. Patchel, *Vogel's Textbook of Organic Chemistry*, Pearson Education Pvt. Ltd, Singapore, 5th edn, 1996, p.1269.

20 E. Knoevengel, Über den Chemismus der condensierenden Wirkung des Ammoniaks und organischer Amine bei Reactionen zwischen Aldehyden und Acetessigester, *Ber. Dtsch. Chem. Ges.*, 1898, **31**, 732–748.

21 D. Bokov, A. Turki Jalil, S. Chupradit, W. Suksatan, M. J. Ansari, I. H. Shewael and G. H. Valiev, 8 and Ehsan Kianfar, Nanomaterial by Sol-Gel Method: Synthesis and Application, *Adv. Mater. Sci. Eng.*, 2021, 1–21.

22 A. C. Scott, J. G. Collee, J. P. Duguid, A. G. Fraser and B. P. Marmion, in *Mackie & McCartney-Practical Medical Microbiology*, Churchill Livingstone, 13th edn, 1989, pp. 161–181.

23 I. Wiegand, K. Hilpert and E. W. H. Robert, Agar and broth dilution methods to determine the minimal inhibitory concentration (MIC) of antimicrobial substances, *Nat. Protoc.*, 2008, **3**(2), 163–175.

24 T. Takao, N. Watanabe, I. Yagi and K. Sakata, A Simple Screening Method for Antioxidants and Isolation of Several Antioxidants Produced by Marine Bacteria from Fish and Shellfish, *Biosci. Biotechnol. Biochem.*, 1994, **58**, 1781–1783, DOI: 10.1271/bbb.58.1780.

25 S. M. Gomha, S. M. Riyadh, E. A. Mahmmoud and M. M. Elaasser, Synthesis and Anticancer Activities of Thiazoles, 1,3-Thiazines, and Thiazolidine Using Chitosan-Grafted-Poly(vinylpyridine) as Basic Catalyst, *Heterocycles*, 2015, **91**(2015), 1227–1243.

26 H. K. Mahmoud, H. A. Abdelhady, M. M. Elaasser, D. Z. H. Hassain and S. M. Gomha, Microwave-Assisted One-Pot Three Component Synthesis of Some Thiazolyl (Hydrazonoethyl) Thiazoles as Potential Anti-Breast Cancer Agents, *Polycyclic Aromat. Compd.*, 2022, **42**, 7232–7246.

27 P. Vijayan, C. Raghu, G. Ashok, S. A. Dhanaraj and B. Suresh, Antiviral activity of medicinal plants of Nilgiris, *Indian J. Med. Res.*, 2004, **120**, 24–29.

28 W. Randazzo, J. Piqueras, J. Rodrıguez-Diaz, R. Aznar and G. Sanchez, Improving efficiency of viability-qPCR for selective detection of infectious HAV in food and water samples, *J. Appl. Microbiol.*, 2018, **124**, 958–964.

29 R. M. Pinto, J. M. Diez and A. Bosch, Use of the colonic carcinoma cell line CaCo-2 for *in vivo* amplification and detection of enteric viruses, *J. Med. Virol.*, 1994, **44**, 310–315.

30 T. Mosmann, Rapid colorimetric assay for cellular growth and survival: Application to proliferation and cytotoxicity assays, *J. Immunol. Methods*, 1983, **65**, 55–63.

31 A. D. Becke, Density-functional exchange-energy approximation with correct asymptotic behavior, *Phys. Rev. A: At., Mol., Opt. Phys.*, 1988, **38**, 3098.

32 M. J. Frisch, G. W. Trucks, H. B. Schlegel, G. E. Scuseria, M. A. Robb, J. R. Cheeseman, G. Scalmani, V. Barone, B. Mennucci, G. A. Petersson, H. Nakatsuji, M. Caricato, X. Li, H. P. Hratchian, A. F. Izmaylov, J. Bloino, G. Zheng, J. L. Sonnenberg, M. Hada, M. Ehara, K. Toyota, R. Fukuda, J. Hasegawa, M. Ishida, T. Nakajima, Y. Honda, O. Kitao, H. Nakai, T. Vreven, J. A. Montgomery Jr, J. E. Peralta, F. Ogliaro, M. Bearpark, J. J. Heyd, E. Brothers, K. N. Kudin, V. N. Staroverov, R. Kobayashi, J. Normand, K. Raghavachari, A. Rendell, J. C. Burant, S. S. Iyengar, J. Tomasi, M. Cossi, N. Rega, J. M. Millam, M. Klene, J. E. Knox, J. B. Cross, V. Bakken, C. Adamo, J. Jaramillo, R. Gomperts, R. E. Stratmann, O. Yazyev, A. J. Austin, R. Cammi, C. Pomelli, J. W. Ochterski, R. L. Martin, K. Morokuma, V. G. Zakrzewski, G. A. Voth, P. Salvador, J. J. Dannenberg, S. Dapprich, A. D. Daniels, O. Farkas, J. B. Foresman, J. V. Ortiz, J. Cioslowski and D. J. Fox, *Gaussian 09, Revision A.02*, Gaussian Inc., Wallingford, CT. 2009.

33 R. Krishnan, J. S. Binkley, R. Seeger and J. A. Pople, Self-consistent molecular orbital methods. XX. A basis set for correlated wave functions, *J. Chem. Phys.*, 1980, **72**, 650–654.

34 P. J. Hay and W. R. Wadt, Ab initio effective core potentials for molecular calculations. Potentials for the transition metal atoms Sc to Hg, *J. Chem. Phys.*, 1985, **82**, 270–283.

35 M. M. Khalaf, H. M. A. El-Lateef, M. Gouda, A. A. Amer, A. A. Abdelhamid, M. F. A. Taleb, A. Alfarsi, T. M. A. Ibrahim, H. El-Shamy and A. Abdou, Synthesis, characterization, DFT, biological activity evaluation, and molecular docking analysis of new 8-[(2-hydroxynaphthalen-1-yl)diazenyl]naphthalene-1,3-disulfonic acid based complexes, *J. Mol. Struct.*, 2024, **1300**, 137175.

36 O. Trott and A. J. Olson, AutoDock Vina: improving the speed and accuracy of docking with a new scoring function, efficient optimization, and multithreading, *J. Comput. Chem.*, 2010, **31**, 455–461.

37 Z. Hussain, M. A. Ibrahim, N. M. Hassanin and A.-S. Badran, Synthetic approaches for novel annulated pyrido [2, 3-d] pyrimidines: Design, Structural Characterization, Fukui functions, DFT Calculations, Molecular docking and Anticancer efficiency, *J. Mol. Struct.*, 2024, **1318**, 139335.

38 A. Zahirović, S. Fetahović, M. Feizi-Dehnayebi, R. Bešta-Gajević, M. Dizdar, J. Ostojić and S. Roca, Substituent effect in salicylaldehyde 2-furoic acid hydrazones: Theoretical and experimental insights into DNA/BSA affinity modulation, antimicrobial and antioxidant activity, *J. Mol. Struct.*, 2024, **1312**, 138628.

39 R. K. Mohapatra, A. Mahal, A. Ansari, M. Kumar, J. P. Guru, A. K. Sarangi, A. Abdou, S. Mishra, M. Aljeldah and B. M. AlShehail, Comparison of the binding energies of approved mpox drugs and phytochemicals through molecular docking, molecular dynamics simulation, and ADMET studies: An *in silico* approach, *Int. J. Biosaf. Biosecur.*, 2023, **5**, 118–132.

40 (*a*) M. Saif, H. F. El-Shafiy, M. M. Mashaly, M. F. Eid, A. I. Nabeel and R. Fouad, Synthesis, characterization, and

antioxidant/cytotoxic activity of new chrome Schiff base nano-complexes of Zn(II), Cu(II), Ni(II) and Co(II), *J. Mol. Struct.*, 2016, **1118**, 75–82; (*b*) R. Fouad, M. A. N. Mahdi and O. M. I. Adly, Selective Metal-Coordinated Nanodrugs Based on Thiazine Moiety for Anticancer Therapeutics: Spectroscopic, Theoretical, and Molecular Docking Studies, *Appl. Organomet. Chem.*, 2025, **39**, e7840.

41 D. S. Ranade, A. M. Bapat, S. N. Ramteke, B. N. Joshi, P. Roussel, A. Tomas, P. Deschamps and P. P. Kulkarni, Thiosemicarbazone modification of 3-acetyl coumarin inhibits Ab peptide aggregation and protect against Ab-induced cytotoxicity, *Eur. J. Med. Chem.*, 2016, **121**, 803–809.

42 N. Salah, A. A. A. Emara, O. M. I. Adly, A. Taha, A. I. Nabeel, M. A. Aziz and M. A. Ibrahim, Novel NO2 semicarbazone ligand and its metal complexes as VEGFR-2 inhibitors: Synthesis, spectral characterization, density functional theory calculations, molecular docking, and antimicrobial and antitumor evaluation, *Appl. Organomet. Chem.*, 2022, **36**, e6845.

43 (*a*) O. M. I. Adly and H. F. El-Shafiy, Synthesis, spectroscopic studies, DFT calculations, antimicrobial and antitumor activity of tridentate NNO Schiff base metal complexes based on 5-acetyl-4-hydroxy-2H-1,3-thiazine-2,6(3H)-dione, *J. Coord. Chem.*, 2019, **72**, 218; (*b*) F. Samy and M. Shebl, Co(II), Ni(II), and Cu(II) complexes of 4,6-bis(2-hydroxynaphthalen-1-yl)methyl-ene)hydrazono)ethyl) benzene-1,3-diol: Synthesis, spectroscopic, biological, and theoretical studies, *Appl. Organomet. Chem.*, 2022, **36**, e6650.

44 R. Fouad, M. Saif, M. M. Mashaly and M. Zekrallah, New Mononuclear Metal Complexes Based on 3- Acetyl- 4- Hydroxy Coumarin as Potential Antitumor Agents: Full Structural Elucidation, Theoretical Calculations, and Biological Activity Studies, *Appl. Organomet. Chem.*, 2025, **39**, e7924.

45 M. Ayad, P. Schollhammer, Y. L. Mest, L. Wojcik, F. Y. Pétillon, N. L. Poul and D. Mandon, Mononuclear copper(II) complexes containing a macrocyclic ditopic ligand: Synthesis, structures and properties, *Inorg. Chim. Acta*, 2019, **497**, 119081.

46 A. A. A. Emara, A. A. Saleh and O. M. I. Adly, Spectroscopic investigations of new binuclear transition metal complexes of Schiff bases derived from 4,6-diacetylresorcinol and 3-amino-1-propanol or 1,3-diamino-propane, *Spectrochim. Acta, Part A*, 2007, **68**, 592.

47 H. G. Sogukomerogullari, E. Basaran, R. A. Kepekçi, B. Türkmenoglu, A. O. Sarıoglu and M. Kose, Novel europium(III), terbium(III), and gadolinium(III) Schiff base complexes: Synthesis, structural, photoluminescence, antimicrobial, antioxidant, and molecular docking studies, *Polyhedron*, 2025, **265**, 117275.

48 S. Y. Ebrahimipour, F. K. Nejad, M. Khosravan, J. Castro, J. M. White, P. Mohammadi, G. Mohamadi-Nejad and M. Mohamadi, Studies on a novel oxo-vanadium(V) complex of a tridentate ONO Schiff base ligand: Synthesis, characterization, X-ray crystal structure, Hirshfeld surface analysis, biological and catalytic activity, *J. Mol. Struct.*, 2025, **1321**, 139923.

49 W. J. Geary, The Use of Conductivity Measurements in Organic Solvents for the Characterization of Coordination Compounds, *Coord. Chem. Rev.*, 1971, **7**, 81.

50 A. W. Coats and J. P. Redfern, Kinetic Parameters from Thermogravimetric Data, *Nature*, 1964, **201**, 68.

51 A. H. M. Siddaligaiah and S. G. Naik, Spectroscopic and thermogravimetric studies on Ni(II), Cu(II) and Zn(II) complexes of di(2,6-dichlorophenyl)carbazone, *J. Mol. Struct.*, 2002, **582**, 129.

52 C. R. Vinodkumar, M. K. Muraleedharan Nair and P. K. Radhakrishnan, Thermal Studies on Lanthanide Nitrate Complexes of 4-n-(2′-furfurylidene) aminoantipyrine, *J. Therm. Anal. Calorim.*, 2000, **61**, 143.

53 M. A. Ibrahim, A. A. A. Emara, A. Taha, O. M. I. Adly, A. I. Nabeel, M. A. Aziz and N. Salah, Synthesis, characterization, TD-DFT, molecular docking, biological applications, and solvatochromic studies of some new metal complexes derived from semicarbazone of pyrano [3,2-c]quinoline-3-carboxaldehyde, *Appl. Organomet. Chem.*, 2023, e7169.

54 M. Saif, M. M. Mashaly, M. F. Eid and R. Fouad, Synthesis, characterization and thermal studies of binary and/or mixed ligand complexes of Cd(II), Cu(II), Ni(II) and Co(III) based on 2-(Hydroxybenzylidene) thiosemicarbazone: DNA binding affinity of binary Cu(II) complex, *Spectrochim. Acta, Part A*, 2012, **92**, 347–356.

55 M. M. Mashaly, Z. H. Abd El-Wahab and A. A. Faheim, Preparation, spectral characterization and antimicrobial activities of Schiff base complexes derived from 4-aminoantipyrine. Mixed ligand complexes with 2-aminopyridine, 8-hydroxyquinoline and oxalic acid and their pyrolytical products, *J. Chin. Chem. Soc.*, 2004, **51**, 901–915.

56 (*a*) K. Nakamoto, *Infrared Spectra of Inorganic and Coordination Compounds*, John Willey & Sons, New York, 5th edn, 1997; (*b*) E. M. Abdelrhman, B. A. El-Shetary, M. Shebl and O. M. I. Adly, Coordinating behavior of hydrazone ligand bearing chromone moiety towards Cu(II) ions: Synthesis, spectral, density functional theory (DFT) calculations, antitumor, and docking studies, *Appl. Organomet. Chem.*, 2021, **35**, e6183.

57 (*a*) M. Shebl, Mononuclear, homo- and hetero-binuclear complexes of 1-(5-(1-(2-aminophenylimino)ethyl)-2,4-dihydroxyphenyl)ethanone: synthesis, magnetic, spectral, antimicrobial, antioxidant, and antitumor studies, *J. Coord. Chem.*, 2016, **69**(2), 199–214; (*b*) O. M. I. Adly, M. Shebl, E. M. Abdelrhman and B. A. El-Shetary, Synthesis, spectroscopic, X-ray diffraction, antimicrobial and antitumor studies of Ni(II) and Co(II) complexes derived from 4- acetyl-5,6-diphenyl-3(2H)-pyridazinone and ethylenediamine, *J. Mol. Struct.*, 2020, **1219**, 128607.

58 O. M. I. Adly, M. Shebl, H. F. El-Shafiy, S. M. E. Khalil, A. Taha and M. A. N. Mahdi, Synthesis, spectroscopic characterization, antimicrobial and antitumor studies of mono-, bi- and tri-nuclear metal complexes of a new Schiff base ligand derived from o-acetoacetylphenol, *J. Mol. Struct.*, 2017, **1150**, 507–522.

59 F. A. Cotton and G. Wilkinson, *Advanced Inorganic Chemistry*, John Wiley, 3rd edn, 1978, p. 541.

60 A. A. M. Ali and R. Fouad, Novel thiosemicarbazone complexes as anticancer agents: Synthesis, characterization, cytotoxicity, docking, and density functional theory studies, *Appl. Organomet. Chem.*, 2024, **38**, e7430.

61 S. A. Al-Thabaiti, A. Y. Obaid, S. Hussain and Z. Khan, Shape-directing role of cetyltrimethylammonium bromide on the morphology of extracellular synthesis of silver nanoparticles, *Arabian J. Chem.*, 2015, **8**, 538–544.

62 J. Gong, W. Zeng and H. Zhang, Hydrothermal synthesis of controlled morphologies of MoO3 nanobelts and hierarchical structures, *Mater. Lett.*, 2015, **154**, 170–172.

63 R. S. Joseyphus and M. S. Nair, Antibacterial and Antifungal Studies on Some Schiff Base Complexes of Zinc (II), *Mycobiology*, 2008, **36**, 93–98.

64 H. F. El-Shafiy, M. F. Eid, M. Saif, M. M. Mashaly, S. Abdel Halim, A. I. Nabeel and R. Fouad, New nano-complexes of Zn(II), Cu(II), Ni(II) and Co(II) ions; spectroscopy, thermal, structural analysis, DFT calculations and antimicrobial activity application, *J. Mol. Struct.*, 2017, **1147**, 452–461.

65 E. Chudáčková, T. Bergerová, K. Fajfrlík, D. Červená, P. Urbášková, J. Empel, M. Gniadkowski and J. Hrabák, Carbapenem-nonsusceptible strains of Klebsiella pneumoniae producing SHV-5 and/or DHA-1 b-lactamases in a Czech hospital, *FEMS Microbiol. Lett.*, 2010, **309**, 62–70.

66 European Committee for Antimicrobial Susceptibility Testing (EUCAST) of the European Society of Clinical Microbiology and Infectious Diseases (ESCMID), Determination of minimum inhibitory concentrations (MICs) of antibacterial agents by broth dilution, *Clin. Microbiol. Infect.*, 2003, **9**, 11–25.

67 H. E. Miller, F. Rigelhof, L. Marquart, A. Prakash and M. Kanter, Antioxidant content of whole grain breakfast cereals, fruits and vegetables, *J. Am. Coll. Nutr.*, 2000, 312S–319S.

68 M. Szymula and J. Narkiewicz-Michalek, Atmospheric and electrochemical oxidation of ascorbic acid in anionic, nonionic and cationic surfactant systems, *J. Colloid Polym. Sci.*, 2003, **281**, 1142–1148.

69 D. Kwasniewska and J. Kiewlicz, Study of interaction between cationic surfactant (CTAB) and ascorbic acid/ascorbic acids derivatives by tensiometric and spectroscopic methods, *J. Mol. Liq.*, 2022, **354**, 118917.

70 Q. Xue, R. Kang, D. J. Klionsky, D. Tang, J. Liu and X. Chen, Copper metabolism in cell death and autophagy, *Autophagy*, 2003, **19**, 2175–2195.

71 Y. Luo, X. Luo, Y. Ru, X. Zhou, D. Liu, Q. Huang, M. Linghu, Y. Wu, Z. Lv, M. Chen, Y. Ma, Y. Huang and J. Wang, Copper (II)-based nano-regulator correlates cuproptosis burst and sequential immunogenic cell death for synergistic cancer immunotherapy, *Biomater. Res.*, 2004, **28**, 0039.

72 P. Huang, G. Wu, M. Huang, Y. Deng, X. Chen, G. Ye, X. Yu, H. Wang, H. Wen and Y. Zhou, Copper-coordinated nanomedicine for the concurrent treatment of lung cancer through the induction of cuproptosis and apoptosis, *Eur. J. Pharm. Sci.*, 2025, **204**, 106942.

73 R. Budzynska, D. Nevozhay, U. Kanska, M. Jagiello, A. Opolski, J. Wietrzyk and J. Boratynski, Antitumor activity of mannan-methotrexate conjugate *in vitro* and *in vivo*, *Oncol. Res.*, 2007, **16**, 415–421.

74 B. Singh, V. Sharma, G. Singh, R. Kumar, S. Arora and M. P. S. Ishar, Synthesis and *In Vitro* Cytotoxic Activity of Chromenopyridones, *Int. J. Med. Chem.*, 2013, **2013**, 984329.

75 R. K. Mohapatra, A. Mahal, A. Ansari, M. Kumar, J. P. Guru, A. K. Sarangi, A. Abdou, S. Mishra, M. Aljeldah, B. M. AlShehail, M. Alissa, M. Garout, A. Alsayyah, A. A. Alshehri, A. Saif, A. Alqahtani, F. A. Alshehri, A. A. Alamri and A. A. Rabaan, Comparison of the binding energies of approved mpox drugs and phytochemicals through molecular docking, molecular dynamics simulation, and ADMET studies: An *in silico* approach, *J. Biosaf. Biosecur.*, 2023, **5**, 118–132.

76 H. M. Abd El-Lateef, M. M. Khalaf, F. El-Taib Heakal and A. Abdou, Fe(III), Ni(II), and Cu(II)-moxifloxacin-tri-substituted imidazole mixed ligand complexes: Synthesis, structural, DFT, biological, and protein-binding analysis, *Inorg. Chem. Commun.*, 2023, **158**, 111486.

77 H. M. Abd El-Lateef, M. M. Khalaf, A. A. Amer, A. A. Abdelhamid and A. Abdou, Antibacterial, antifungal, anti-inflammatory evaluation, molecular docking, and density functional theory exploration of 2-(1H-benzimidazol-2-yl)guanidine mixed-ligand complexes: Synthesis and characterization, *Appl. Organomet. Chem.*, 2024, **38**, e7299.

78 H. M. Abd El-Lateef, M. M. Khalaf, F. E. T. Heakal and A. Abdou, Fe (III), Ni (II), and Cu (II)-moxifloxacin-tri-substituted imidazole mixed ligand complexes: Synthesis, structural, DFT, biological, and protein-binding analysis, *Inorg. Chem. Commun.*, 2023, **158**, 111486.

79 W. Derafa, N. A. Elkanzi, A. M. Ali and A. Abdou, Three Co (II), Ni (II) and Cu (II) Schiff base complexes incorporating 2-[(4-{[(4-methylphenyl) sulfonothioyl] oxy} phenyl) methylene] amino} benzoic acid: Synthesis, structural, dft, biological and molecular docking investigation, *Bull. Chem. Soc. Ethiop.*, 2024, **38**, 325–346.

80 A. Abdou, H. Mostafa and A.-M. Abdel-Mawgoud, New Fe(III) and Ni(II) Azocoumarin Based Complexes: Synthesis, Characterization, DFT, Antimicrobial, Anti-inflammatory Activity, and Molecular Docking Analysis, *Russ. J. Gen. Chem.*, 2023, **93**, 3006–3019.

81 T. Lanez, M. Feizi-Dehnayebi and E. Lanez, Assessment of the electrostatic binding of ferrocenylmethyl-nitroaniline derivatives to DNA: A combined experimental and theoretical study, *J. Mol. Struct.*, 2024, **1308**, 138386.

82 S. Cherukupalli, B. Chandrasekaran, R. R. Aleti, N. Sayyad, G. A. Hampannavar, S. R. Merugu, H. R. Rachamalla, R. Banerjee and R. Karpoormath, Synthesis of 4,6-disubstituted pyrazolo[3,4-d]pyrimidine analogues: Cyclin-dependent kinase 2 (CDK2) inhibition, molecular docking and anticancer evaluation, *J. Mol. Struct.*, 2019, **1176**, 538–551.